Tracing the phase boundaries of hard spherocylinders

Peter Bolhuis and Daan Frenkel
FOM Institute for Atomic and Molecular Physics, Kruislaan 407, 1098 SJ Amsterdam, The Netherlands

(Received 4 June 1996; accepted 26 September 1996)

We have mapped out the complete phase diagram of hard spherocylinders as a function of the shape anisotropy L/D. Special computational techniques were required to locate phase transitions in the limit $L/D\rightarrow\infty$ and in the close-packing limit for $L/D\rightarrow 0$. The phase boundaries of five different phases were established: the isotropic fluid, the liquid crystalline smectic A and nematic phases, the orientationally ordered solids—in AAA and ABC stacking—and the plastic or rotator solid. The rotator phase is unstable for $L/D\geqslant 0.35$ and the AAA crystal becomes unstable for lengths smaller than $L/D\approx 7$. The triple points isotropic-smectic-A-solid and isotropic-nematic-smectic-A are estimated to occur at $L/D = 3.1$ and $L/D = 3.7$, respectively. For the low L/D region, a modified version of the Gibbs–Duhem integration method was used to calculate the isotropic-solid coexistence curves. This method was also applied to the I-N transition for $L/D>10$. For large L/D the simulation results approach the predictions of the Onsager theory. In the limit $L/D\rightarrow\infty$ simulations were performed by application of a scaling technique. The nematic-smectic-A transition for $L/D\rightarrow\infty$ appears to be continuous. As the nematic-smectic-A transition is certainly of first order nature for $L/D\leqslant 5$, the tri-critical point is presumably located between $L/D=5$ and $L/D=\infty$. In the small L/D region, the plastic solid to aligned solid transition is first order. Using a mapping of the dense spherocylinder system on a lattice model, the initial slope of the coexistence curve could even be computed in the close-packing limit. [S0021-9606(97)51901-5]

I. INTRODUCTION

Intuitively, one associates increased order with a decrease in entropy. It is therefore surprising that a large number of phase transitions exist in which both the structural order and the entropy of the system increase. In particular, all ordering transitions in systems of particles that have exclusively hard-core interactions are of this type. Already in the forties, Onsager showed[1] that thin hard rods must form a nematic liquid crystal at sufficiently high densities. In the fifties, the computer-simulation studies of Alder and Wainwright, and Wood and Jacobson[2,3] provided the first conclusive evidence that hard spherical particles undergo a first order freezing transition. Subsequently, computer simulations of a variety of models of nonspherical hard-core models showed that excluded volume effects could not only account for the stability of nematics,[4,5] but also for the existence of smectic[6–9] and columnar[10,11] liquid-crystalline phases (for a review, see Ref. 12).

The study of such simple hard-core models would, at first sight, seem to be of purely academic interest. However, simulations of hard particles turn out to be of considerable practical relevance for the study of colloidal materials consisting of anisometric inorganic colloids[13] or rodlike virus particles.[14] To a first approximation, hard spherocylinders (cylinders of length L and diameter D capped with two hemispheres at both ends) provide a good model for rodlike colloidal particles with short-ranged repulsive interactions. The parameter that characterizes the phase behavior of such particles is the shape anisotropy L/D. Note that the length-to-width ratio of spherocylinders is given by $L/D+1$. Using this notation, hard spheres have a length-to-width ratio of 1 but a shape anisotropy $L/D=0$. In this paper, we mainly use the shape anisotropy parameter.

Of course, the behavior of real rodlike colloids may differ from that of rigid hard spherocylinders, either because the colloid–colloid interaction is not truly a hard-core repulsion or because real colloids are never completely rigid. It is clearly of interest to know where the analogy between real colloids and the corresponding hard-core model breaks down. However, in order to detect such differences in behavior, it is obviously important to have a good knowledge of the hard-spherocylinder (HSC) phase diagram over a wide range of L/D values.

A first attempt to map out the HSC phase diagram was reported by Veerman and Frenkel.[9] However, this study focused on only a small number of rather widely spaced L/D values. As a consequence, the phase boundaries for intermediate L/D values could only be sketched, while some phase boundaries were not studied at all. This situation is clearly unsatisfactory, as the HSC system is now often used as a reference system to compare both with experiment and with theory. For precisely this reason, McGrother *et al.*[15] recently performed more extensive simulations in the region $3<L/D<5$. The aim of the present paper is to compute the *complete* phase diagram of the spherocylinder model (i.e., from $L/D=0$ to $L/D=\infty$, and from low density to close packing). In order to achieve this, we employ several computational techniques that have been developed in the past few years that enable us to map the HSC phase diagram over a wide range of L/D values.

In this study we pay special attention to three aspects of the phase diagram. The first is the location of the orientational order–disorder transition in the solid (for small ani-

 0021-9606/97/106(2)/666/22/$10.00

sometries). This transition has, thus far, not been studied for spherocylinders. More interestingly, using a novel computational technique,[16] we are now able to trace the coexistence curve between rotator phase and orientationally ordered crystal all the way to close packing. Second, we are interested in the behavior of spherocylinders for large L/D and in particular the Onsager limit. The third point of special interest is the location of the triple points in the phase diagram. Specifically, there is a maximum L/D value beyond which no crystalline rotator phase can exist and similarly, there are lower limits for L/D below which the smectic, nematic, and the crystalline AAA phases become thermodynamically unstable.

Veerman and Frenkel[9] made no attempt to estimate the first triple point and could only give rather wide margins for the latter three. In particular, they found that whereas rods with a shape anisotropy $L/D=5$ can form both a stable nematic and a stable smectic phase, at $L/D=3$ the smectic phase is only meta-stable while the nematic phase is even mechanically unstable. Clearly, the only conclusion that could be drawn from the simulations in Ref. 9 is that the triple points that terminate the range of nematic and smectic stability must be located somewhere between $L/D=3$ and $L/D=5$. But it remained unclear where exactly this would happen and which triple point would come first.

Moreover, one should expect the nematic-smectic transition to be first order for small L/D values and continuous for long spherocylinders. Different theories make different predictions about the location of the tricritical point: in Refs. 17 and 18 it is estimated that the tricritical point corresponds to $L/D\approx 5$ while the theoretical analysis in Ref. 19 suggests that it should occur at $L/D=50$. The present simulations strongly suggest that this tri-critical point occurs at an L/D value appreciable larger than 5, but are not suited to determine the exact location of the tri-critical point.

The recent NPT Monte Carlo simulations of McGrother *et al.*[15] were performed on a system of spherocylinders with an L/D range of 3–5. They found that the isotropic-smectic triple point occurs at $L/D\approx 3.2$ and that the isotropic-nematic-smectic triple point is located around $L/D=4$. Further, they also found evidence for a first order nematic-smectic transition at $L/D=5$.

The outline of the remainder of this paper is as follows. For readers who are less interested in the technical details of the simulations, Sec. II summarizes the main results concerning the phase behavior of spherocylinders. Subsequently, different aspects of the simulations are discussed in some detail. Section III describes the simulation techniques and the methods we used to calculate the free energy of the different phases. In particular, Sec. III C describes how we have modified the so-called Gibbs–Duhem integration technique of Kofke[20] to trace the melting curve for $0.4\leqslant L/D\leqslant 3$. The results for $L/D<5$ are presented in Sec. IV. The location of the first order transition between solid and rotator is discussed in Sec. V. This section also describes the computational technique used to study this transition in the limit of close packing of the spherocylinders. In Sec. VI results for long rods (up to $L/D=60$) are presented. The isotropic-nematic transition is studied both by Gibbs-ensemble simulation and Gibbs–Duhem integration. For $L/D\rightarrow\infty$ this transition is expected to approach the behavior predicted by the Onsager theory. We discuss the nematic-smectic and smectic solid transitions for long rods ($L/D=40$). We also present a rough estimate for the AAA phase boundaries in this section. Finally, in Sec. VII the simulation of spherocylinders in the limit $L/D\rightarrow\infty$ are discussed.

II. BRIEF SUMMARY OF THE PHASE DIAGRAM

A. Phase diagram for $L/D\leqslant 5$

Figure 1 shows the computed phase diagram of hard spherocylinders in the region between $L/D=0$ (hard spheres) and $L/D=5$. The black squares indicate the reduced transition densities for L/D values at which simulations were performed. In this and following figures, the reduced density $\rho^*=\rho/\rho_{\rm cp}$ is the density relative to the density of regular close packing of spherocylinders:

$$\rho_{\rm cp}=2/(\sqrt{2}+(L/D)\sqrt{3}).$$

For particles with $L/D\leqslant 0.35\pm 0.05$, the isotropic fluid freezes to form a plastic crystal (rotator phase). At higher densities, the rotator phase undergoes a first order transition to the orientationally ordered phase. As L/D is lowered to zero, this transition moves toward the density of regular close packing $\rho^*=1$.

Between $L/D=0.35$ and $L/D=3.1$, only two phases occur: the low-density isotropic phase and the high-density, orientationally ordered, crystal phase. The smectic phase first becomes stable at the I-SmA-S triple point which is located at $L/D=3.1$. The nematic phase becomes stable at $L/D=3.7$. The nematic-smectic transition takes place around $\rho^*=0.5$ and is initially clearly first order, but the density jump at the N-S transition shrinks with increasing L/D. The smectic to solid transition is located at $\rho^*=0.66-0.68$ and is also first order.

B. Phase diagram for $L/D>5$

In Fig. 2, the phase behavior for long rods is depicted as a function of $\log(L/D+1)$ to give equal emphasis to the different parts of the phases diagram. For larger values of L/D, the I-N transition moves to lower densities and the density jump at the I-N transition, which is too small to be measured for rods with $L/D\leqslant 5$, increases to almost 20%, as $L/D\rightarrow\infty$, as predicted by Onsager theory. In contrast, the density of the nematic-smectic transition is not very sensitive to the shape anisotropy of the rods and approaches the finite limit $\rho^*=0.47$ as $L/D\rightarrow\infty$. Similarly, the smectic-to-solid transition exhibits only a weak dependence on L/D and occurs still at $\rho^*\approx 0.66$ in the $L/D\rightarrow\infty$ limit.

At L/D values greater than approximately 7 a crystal phase with an AAA stacking becomes stable between the smectic and the ABC stacked solid. This crystal phase is characterized by hexagonal planes which are stacked precisely on top of each other. At higher density the ABC stacked solid, which has the hexagonal planes shifted with

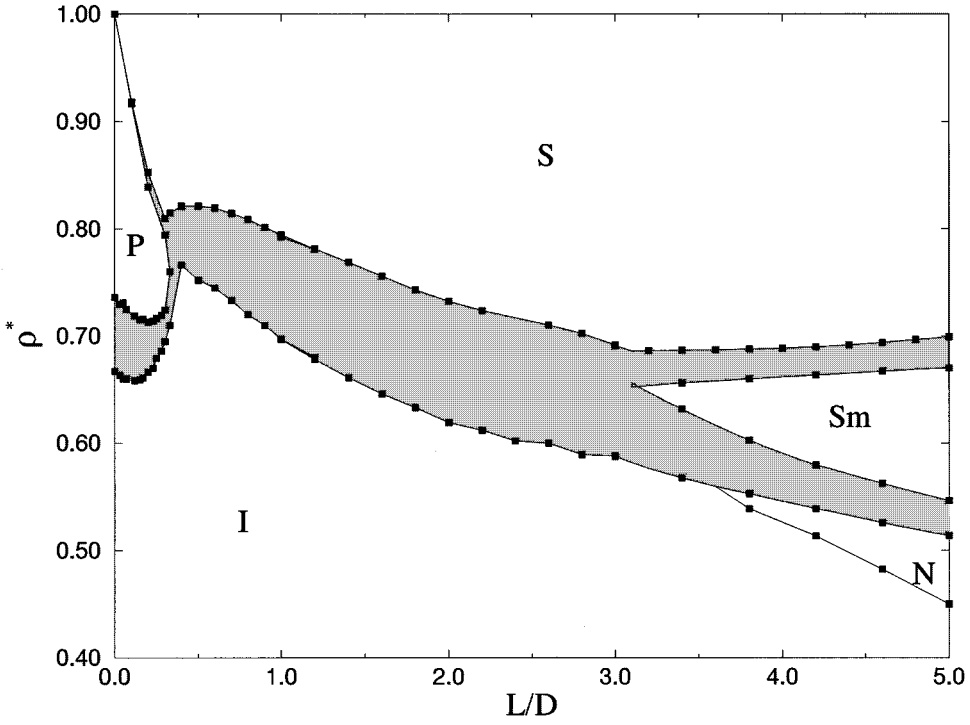

FIG. 1. Phase diagram for hard spherocylinders of aspect ratio $L/D<5$. All two-phase regions are shown shaded. In the figure, the following phases can be distinguished: the low-density isotropic liquid, the high-density orientationally ordered solid, the low-L/D plastic solid and, for $L/D>3.7$, the nematic and smectic-A phases.

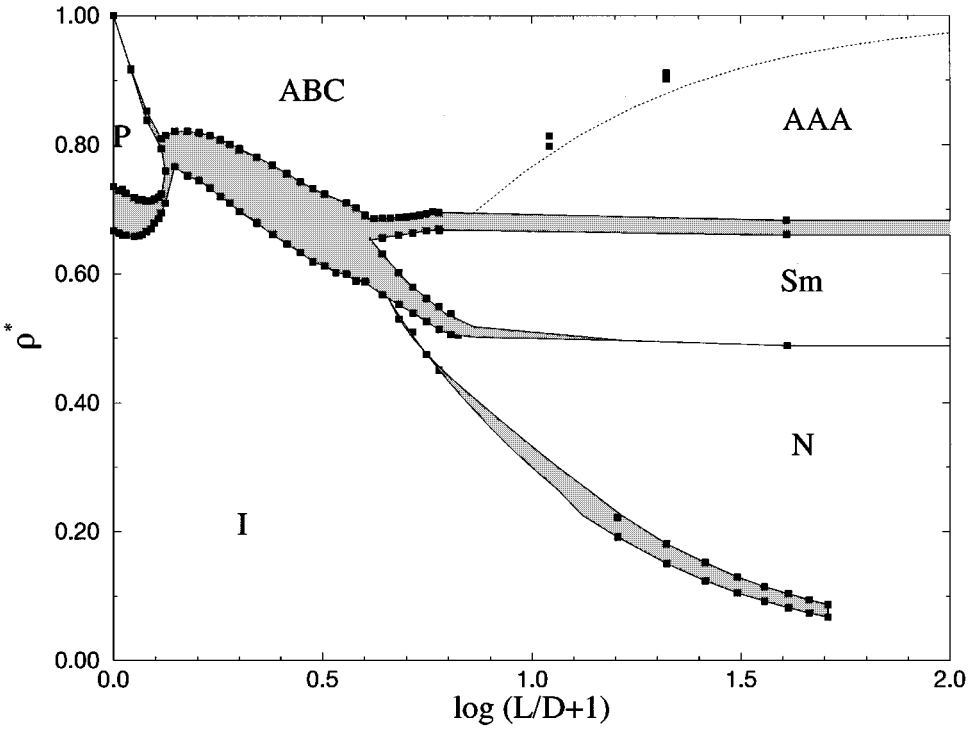

FIG. 2. Summary of the phase diagram of hard spherocylinders with L/D between 0 and 100. In order to give equal emphasis to all parts of the phase diagram, we have plotted ρ^* as a function of $\log(L/D+1)$. The dashed line is a crude estimate for the first order AAA-ABC transition as given in Eq. (52).

respect to each other, will still be the most stable structure. The density of the AAA-ABC transition increases quickly for $L/D>7$ to reach the close-packing limit at $L/D\rightarrow\infty$.

More details on the phase behavior of long spherocylinders can be found in Sec. VI.

III. SIMULATION TECHNIQUES

A. Equilibration

Knowledge of the equation of state often provides a rough estimate of the limits of stability of the various phases. By starting with different configurations at different densities the range of mechanical stability of the observed phase can be estimated. If only one phase is mechanically stable at a given density, this will also be the thermodynamically stable phase. If more phases appear to be stable at the same density, a free-energy calculation is necessary to identify the one that is thermodynamically stable.

In our simulation studies of the equation of state of hard spherocylinders, we generated initial conditions both by expansion and by compression. Specifically, we prepared the configurations of a (dense) spherocylinder system in the following ways

- *Expansion of a solid phase.* A close-packed fcc lattice of spheres with its (111) plane in the xy plane was stretched in the z direction by a factor of $(L/D+1)$ in order to accommodate a close-packed crystal of spherocylinders. This ABC-stacked lattice was subsequently expanded to the desired density and allowed to equilibrate. In the crystalline and smectic phases, the box shape should have the freedom to fluctuate in order to obtain an isotropic pressure. In those cases, we used variable-shape constant-volume Monte Carlo (VSMC). Otherwise, simple constant-volume Monte Carlo was employed.
- *Compression of an isotropic liquid phase.* At low density an ABC-stacked lattice of spherocylinders was allowed to melt into an isotropic liquid using NVT Monte Carlo. This configuration was subsequently compressed to the desired density using constant-NPT Monte Carlo and allowed to equilibrate again with constant-NVT Monte Carlo.
- *Starting from a smectic configuration.* In studying the smectic-to-nematic transition and the smectic-to-solid transition, it is preferable to start with a stacking of hexagonal ordered layers and let this equilibrate by VSMC. The configuration obtained was subsequently compressed by NPT MC or expanded and allowed to equilibrate again.
- *Starting from a nematic configuration.* In studying the nematic-smectic transition by compression, it is preferable to start with a defect-free nematic phase. However, the nematic phase that forms upon compression of the isotropic liquid usually contains long-lived defects. To prepare a defect-free nematic phase, we first generated a hexagonal crystal lattice (AAA stacking) at a density where the nematic phase is known to be the stable one. From this configuration, we first prepare an aligned columnar phase, by displacing every column in the hexagonal crystal by a random shift along the z axis. Subsequently, we allowed the spherocylinders to rotate but not yet translate in order to suppress an initial fast relaxation to the smectic phase. After a few thousand cycles translation was allowed as well and the system was allowed to equilibrate. The equilibrated nematic configuration was compressed by NPT MC to the desired density and equilibrated again. In principle, we kept the box shape fixed in the nematic phase. However, close to the smectic phase boundary, where appreciable smectic fluctuations are already present in the system, we found it advantageous to use VSMC even in the nematic phase, to speed up equilibration.

It should be noted that for insufficiently equilibrated systems, defect structures may occur in the nematic and smectic phases. Defects in the nematic phase, for instance, have been studied by Hudson *et al.*[21] In addition, there may be an equilibrium concentration of point defects in the smectic phase.[22] In the present study we have not investigated the defect structures in the different phases.

After preparing well-equilibrated configurations of the various phases, we used molecular dynamics simulations to measure the pressure of the system using the method described in Refs. 23 and 24. Occasionally, we also used molecular dynamics to speed up the equilibration. This proved to be particularly useful near the nematic-smectic transition where equilibration involves collective rearrangements of large numbers of particles—something that is not easily achieved using single-particle Monte Carlo moves. Whenever MD simulations are performed, we choose the mass m of the spherocylinder as our unit of mass, and hence the unit of time is $\tau\equiv D\sqrt{m/kT}$. The moment of inertia was computed, assuming a uniform mass distribution in the spherocylinder. The MD simulations that we used to measure the pressure in a well-equilibrated system were typically of 2000 collisions per particle.

The number of particles we used to calculate different parts of the equation of state and the length of a typical simulation are summarized in Table I. To study the equation of state in the isotropic and solid phases for low L/D values, relatively small systems could be used [$\mathcal{O}(10^2)$ particles]. For the meso-phases it was often necessary to go to larger systems [($\mathcal{O}(10^3)$ particles].

B. Free-energy calculations

In order to locate first order transitions, accurate free-energy values are necessary. For our computation of the coexistence curves between the different phases as a function of L/D, we calculate the free energy of the isotropic, nematic, smectic, and solid phases by means of thermodynamic integration. This method links the original system for which we want to know the absolute free energy to a reference state of known free energy via a reversible path. If the path is denoted by parameter λ we can define $F(\lambda=0)$ as the free

TABLE I. Simulation parameters for the various parts of the phase diagram of hard spherocylinders. I stands for isotropic, N for nematic, Sm for smectic, R for rotator, and S for solid (ABC) phase. The column MC gives the total number of Monte Carlo cycles; the column MD the number of collisions per particle during a MD simulation. Gibbs–Duhem integrations have two numbers at N_{part} column, because both phases are simulated simultaneously

L/D (increment)	Type	Phase	ρ^* range	N_{part}	MC ($\times 10^5$)	MD ($\times 10^3$)
0.01	compression	R-S	0.982–0.994	144	1	20
	expansion	R-S	0.992–0.996	144	1	20
0.1	compression	R-S	0.80–0.96	144	1	4
	expansion	R-S	0.92–0.98	144	1	4
0.2	compression	R-S	0.76–0.90	144	1	4
	expansion	R-S	0.82–0.98	144	1	4
0.3	compression	R-S	0.70–0.84	144	1	4
	expansion	R-S	0.80–0.98	144	1	4
0.0–0.3 (0.025)	Gibbs–Duhem	I-R	-	200/240	-	1
0.4–3.0 (0.2)	Gibbs–Duhem	I-S	-	200/240	-	1
3.0–5.0 (0.4)	compression	I	0.20–0.54	512	8	2
	compression	I-N	0.40–0.60	512	4	2
	expansion	I-N	0.40–0.60	512	4	2
	compression	N-Sm	0.54–0.60	512	3	2
	expansion	N-Sm	0.54–0.66	540	10	2
	compression	Sm-S	0.64–0.72	336	4	2
	expansion	Sm-S	0.62–0.72	336	4	2
	expansion	S	0.66–0.90	144	2	2
15–50 (5)	Gibbs–Duhem	I-N	-	480/480	-	0.5
40	expansion	I-N	0.05–0.15	2950	-	0.5
	compression	N-Sm	0.46–0.58	1980	2	1
	expansion	N-Sm	0.46–0.66	1980	4	2
	expansion	Sm-S	0.60–0.76	504	2	2

energy of the original system and $F(\lambda=1)$ as the known free energy of the reference system. Integration along the path yields

$$F_{\lambda=1}-F_{\lambda=0}=\int_0^1\left(\frac{\partial F}{\partial\lambda}\right)_{\mathrm{NVT}\lambda}d\lambda. \tag{1}$$

1. Isotropic and nematic phases

For the isotropic phase we can take the ideal gas as a reference and integrate along the equation of state using the density ρ as the integration parameter

$$\frac{F(\rho,L)}{N}-\frac{F_{\mathrm{id}}(\rho)}{N}=\int_0^{\rho}\frac{P(\rho',L)-\rho'}{\rho'^2}\,d\rho'. \tag{2}$$

Because the isotropic-nematic transition shows only a very small density jump at low L/D, it is possible to extend the integration through the transition and obtain the free energy of the nematic phase as well.

2. Solid phase

The strong first order transition separating the solid phase from the other phases rules out the integration along the equation of state. Instead, we choose as a reference system for the solid an Einstein crystal with the same structure.[25] Now the reversible path transforms the original system to an Einstein crystal with fixed center-of-mass, by gradually coupling the atoms to their equilibrium lattice position. For the hard-spherocylinder system the orientation also needs to be coupled to an aligning field. The Hamiltonian that we use to achieve the coupling is the same as given in Ref. 9:

$$\beta H_{\mu,\lambda}=\mu\sum_i(\mathbf{r}_i-\mathbf{r}_i^0)^2+\lambda\sum_i\sin^2\theta_i, \tag{3}$$

where μ and λ are the coupling constants which determine the strength of the harmonic forces. The free energy of the HSC system can be related to the (known) free energy of an Einstein crystal by thermodynamic integration

$$\frac{\beta F(\rho^*)}{N}=\frac{\beta F_{\mathrm{ein}}}{N}-\int_0^{\mu_{\max}}d\mu\langle\Delta r^2\rangle_\mu-\int_0^{\lambda_{\max}}d\lambda\langle\sin^2\theta\rangle_\lambda-\frac{\ln V}{N}. \tag{4}$$

Here $\langle\Delta r^2\rangle_\mu$ is the mean-square displacement and $\langle\sin^2\theta\rangle_\lambda$ the mean-square sine of the angle between a particle and the aligning field in a simulation with Hamiltonian $H_{\mu,\lambda}$. The free energy of the Einstein crystal (with fixed center-of-mass) in the limit of large coupling constants is given by

$$\beta F_{\mathrm{ein}}=\frac{3}{2}\ln N-\frac{3}{2}(N-1)\ln\frac{\pi}{\mu}-N\ln\frac{2\pi}{\lambda}. \tag{5}$$

By performing several simulations at different values of μ and λ, one can numerically evaluate the integrals in Eq. (4). As the values μ and λ at which the integrand is evaluated can be chosen freely, the error in the integration can be minimized by using Gauss–Legendre quadrature. Occurrence of

any first order transition was avoided by performing two Gauss–Legendre integrations in succession. The first fixes the positions while leaving $\lambda=0$; the second aligns all spherocylinders while keeping $\mu=\mu_{\max}$. It is convenient to choose the maximum values of λ and μ such that in a simulation at these maximum values, there are essentially no overlaps between the particles. Otherwise it is necessary to correct Eq. (5) for the occurrence of overlaps.[5]

3. Smectic phase

The smectic phase does not have an obvious reference state for which the free energy is known. Veerman[9] used the parallel spherocylinder system as a reference. However, the free energy of a parallel smectic itself is subject to numerical error. We chose to couple the spherocylinders with an harmonic spring to the smectic layer to which they belong and subsequently align them. In this way, the smectic phase can be transformed into what is essentially a 2D hard disk fluid for which the free energy is well known.[26] In principle, one could apply the Einstein integration method used in the previous section with one difference: the position field couples only the z coordinates of the particles to the layer positions and leaves the x,y coordinates completely free. If we consider the first part of the integration, where the particle are confined to their layers, the free energy of smectic phase can be related to this planar system by

$$\frac{\beta F_{\mu=0}}{N}=\frac{\beta F^{\text{planar}}_{\mu=\mu_0}}{N}-\int_0^{\mu_0} d\mu\langle\Delta r^2\rangle_\mu-\frac{\ln V}{N}. \tag{6}$$

In the second integration, the difficulty arises that an infinite amount of aligning energy is needed to get all spherocylinders completely parallel:

$$\frac{\beta F^{\text{planar}}_{\lambda=0,\mu=\mu_0}}{N}=\frac{\beta F^{\text{planar,aligned}}_{\lambda=\infty,\mu=\mu_0}}{N}-\int_0^{\infty} d\lambda\langle\sin^2\ \theta\rangle_\lambda\,. \tag{7}$$

To keep the energy values finite, we subtract on both sides of this equation the free energy of an ideal rotator in the same field:

$$\frac{\beta F^{\text{planar,id}}_{\lambda=\lambda_0,\mu=\mu_0}}{N}=\frac{\beta F^{\text{planar,aligned,id}}_{\lambda=\infty,\mu=\mu_0}}{N}-\int_{\lambda_0}^{\infty} d\lambda\langle\sin^2\ \theta\rangle_{\text{id},\lambda}\,, \tag{8}$$

which results in

$$\begin{aligned}\frac{\beta F^{\text{planar}}_{\lambda=0,\mu=\mu_0}}{N}=&\frac{\beta F^{\text{planar,id}}_{\lambda=\lambda_0,\mu=\mu_0}}{N}+\frac{\beta F^{\text{planar,aligned,ex}}_{\lambda=\infty,\mu=\mu_0}}{N}\\&-\int_0^{\lambda_0} d\lambda\langle\sin^2\ \theta\rangle_\lambda\\&-\int_{\lambda_0}^{\infty} d\lambda[\langle\sin^2\ \theta\rangle_\lambda-\langle\sin^2\ \theta\rangle_{\text{id},\lambda}].\end{aligned} \tag{9}$$

The excess free energy of the completely aligned planar system $\beta F^{\text{planar,aligned,ex}}_{\lambda=\infty,\mu=\mu_0}$ is equal to the excess free energy of a 2D hard disk fluid. The free energy of the ideal planar system (with fixed center-of-mass) in the limit of large coupling constants is given by

$$\beta F^{\text{planar,id}}_{\lambda=\lambda_0,\mu=\mu_0}=\frac{1}{2}\ln N-\frac{1}{2}(N-1)\ln\frac{\pi}{\mu}-N\ln\frac{2\pi}{\lambda}. \tag{10}$$

The integral over the difference of the $\sin^2$ terms in Eq. (9) is finite. We can change the integration boundaries by substituting $\lambda=1/\xi^2$:

$$\begin{aligned}&\int_{\lambda_0}^{\infty} d\lambda[\langle\sin^2\ \theta\rangle_\lambda-\langle\sin^2\ \theta\rangle_{\text{id},\lambda}]\\&=\int_0^{1/\sqrt{\lambda_0}} d\xi 2\lambda^{2/3}[\langle\sin^2\ \theta\rangle_\lambda-\langle\sin^2\ \theta\rangle_{\text{id},\lambda}].\end{aligned} \tag{11}$$

In conventional MC sampling, the statistical error of both terms in the integrand is larger than the difference itself. We therefore applied the following scheme to evaluate the difference directly in the Monte Carlo program. Instead of rotating a spherocylinder i around an angle $d\theta_i$ we choose a completely new trial value of θ_i from the probability distribution:

$$P(\theta)\sim\exp(-\beta\lambda\ \sin^2\ \theta). \tag{12}$$

This is the equilibrium distribution for an ideal rotator with a Hamiltonian according to Eq. (3) and results in the correct value for $\langle\sin^2\theta\rangle_{\text{id},\lambda}$. If no overlap occurs the trial move will be accepted and we will have

$$\sin^2_\lambda\ \theta_i-\sin^2_{\text{id},\lambda}\ \theta_i=0. \tag{13}$$

If an overlap does occur, the trial move will be rejected and the particle will retain its old value. The difference now will be

$$\sin^2_\lambda\ \theta_i-\sin^2_{\text{id},\lambda}\ \theta_i=\sin^2_\lambda\ \theta_i^{\text{old}}-\sin^2_{\text{id},\lambda}\ \theta_i^{\text{new}}. \tag{14}$$

The statistical error in the average of the difference is always smaller than the average itself. This will enable us to determine the integrand more accurately. By combining Eqs. (6), (9), and (11), the complete expression for free energy of the smectic phase follows

$$\begin{aligned}\frac{\beta F_{\mu=0}}{N}=&\frac{\beta F^{\text{ex}}_{\text{disk}}}{N}-\frac{\beta F^{\text{planar,id}}_{\lambda=\lambda_0,\mu=\mu_0}}{N}-\frac{\ln V}{N}\\&-\int_0^{\mu_0} d\mu\langle\Delta r^2\rangle_\mu-\int_0^{\lambda_0} d\lambda\langle\sin^2\ \theta\rangle_\lambda\\&-\int_0^{1/\sqrt{\lambda_0}} d\xi 2\lambda^{2/3}[\langle\sin^2_\lambda\ \theta-\sin^2_{\text{id}\lambda}\ \theta\rangle].\end{aligned} \tag{15}$$

The excess hard disk free energy can be obtained by subtracting the ideal term $\beta F^{\text{id}}_{\text{disk}}=\ln\rho$ from the free energy in Ref. 26. All integrations were carried out using Gauss–Legendre quadrature. To ensure that the 2D densities in the smectic layers are equal throughout the system, we used shifted periodic boundaries. In our system the periodic boundaries in the x direction are shifted exactly one layer

period along the z axis, while leaving them the same in the y and z direction. In this way, a particle leaving the simulation box at the left side will reenter the box at the right *one layer higher*. This particle can diffuse through the whole system, as there is effectively only one layer. This ensures that fluctuations in the number of particles per smectic layer can relax, even at high density where normal inter-layer diffusion is effectively frozen out.

4. Nematic-smectic free-energy difference

It turned out to be rather difficult to determine the first order nematic-smectic coexistence region for $L/D<5$, because the location of the coexistence point appeared to be quite sensitive to errors in the free energy of the nematic and smectic phases. Therefore, we calculated the free-energy difference between a stable nematic and a stable smectic directly. In order to find a reversible path from the nematic to smectic we applied the following Hamiltonian

$$H_\lambda = \lambda\left(\sum_i \cos\left(\frac{2\pi n r_{i,z}}{L_z}\right)+1\right), \tag{16}$$

where n is the number of smectic layers, L_z the box length in the z direction, $r_{i,z}$ the z coordinate of particle i, and λ the coupling parameter determining the strength of the smectic ordering. At low density this Hamiltonian will produce, by increasing λ, a gradual transition from a nematic to a smectic phase. We started with a smectic phase and applied a cosine field at large enough λ. Subsequently, the smectic was expanded to lower density, while measuring the pressure. Finally, the cosine field was slowly turned off. The free-energy difference now simply is

$$\begin{aligned}\frac{\Delta F_{\rm ns}}{N} &= \frac{F_{\rm smec}}{N} - \frac{F_{\rm nem}}{N} \\ &= \int_0^{\lambda_{\max}} d\lambda \left\langle \sum_i \cos\left(\frac{2\pi n r_{i,z}}{L_z}\right)+1 \right\rangle_{\rm smec} \\ &\quad - \int_{\rho_n}^{\rho_s} \frac{P(\rho)}{\rho^2}\, d\rho \\ &\quad - \int_0^{\lambda_{\max}} d\lambda \left\langle \sum_i \cos\left(\frac{2\pi n r_{i,z}}{L_z}\right)+1 \right\rangle_{\rm nem}.\end{aligned} \tag{17}$$

Of course, the value of $\lambda_{\max}$ should be chosen large enough that the first order S-N transition is completely suppressed.

5. Kappa integration

It is not necessary to perform free-energy calculations for all values of L/D. Once the free energy of a phase at certain density and L/D is established the free energy at other values of L/D can be obtained by a simple thermodynamic integration scheme. We can compute the reversible work involved in changing the aspect ratio of the spherocylinders from L_0 to L and subsequently changing the density from ρ_0 to ρ (temporarily setting $D=1$):

$$\frac{F(\rho,L)}{N} = \frac{F_0(\rho_0,L_0)}{N} + \int_{L_0}^{L}\left(\frac{\partial F}{\partial L}\right)_{\rho_0} dL + \int_{\rho_0}^{\rho}\frac{P(\rho,L)}{\rho^2}\, d\rho. \tag{18}$$

Here we have set $D=1$ for convenience. The $F_0(\rho_0,L_0)$ has to be determined by free-energy calculations as described above. The pressure is obtained from an MD simulation in the usual way, by time averaging the virial:

$$\frac{\beta P}{\rho} - 1 = \frac{1}{3}\beta \sum_{i\leqslant j} \langle \mathbf{f}_{ij}\cdot\mathbf{r}_{ij}\rangle, \tag{19}$$

where $\mathbf{r}_{ij}$ is the vector joining the centers-of-mass of particles i and j, and $\mathbf{f}_{ij}$ denotes the (impulsive) force on j due to i. The derivative $\kappa=(\partial F/\partial L)_\rho$ can be measured at the same time by taking the projection of the intermolecular force along the particle axis:

$$\kappa = \left(\frac{\partial F}{\partial L}\right)_\rho = \frac{1}{2}\sum_{ij} \langle \mathbf{f}_{ij}\cdot(\mathbf{u}_i+\mathbf{u}_j)\rangle. \tag{20}$$

The average κ is calculated at constant number density ρ. However, it is more convenient to measure it at constant reduced density ρ^* (i.e., at a constant fraction of the close-packing density). If we denote this derivative by κ', we get

$$\begin{aligned}\kappa' = \left(\frac{\partial F}{\partial L}\right)_{\rho^*} &= \left(\frac{\partial F}{\partial L}\right)_\rho + \left(\frac{\partial F}{\partial \rho}\right)_L \left(\frac{\partial \rho}{\partial L}\right)_{\rho^*} \\ &= \left(\frac{\partial F}{\partial L}\right)_\rho - \frac{\sqrt{3}}{2\rho^*} P(\rho^*,L),\end{aligned} \tag{21}$$

and Eq. (18) becomes

$$\begin{aligned}F(\rho^*,L) = F_0(\rho_0,L_0) &+ \int_{L_0}^{L} dL\left(\left(\frac{\partial F}{\partial L}\right)_\rho - \frac{\sqrt{3}}{2\rho^*}P(\rho^*,L)\right) \\ &+ \int_{\rho_0}^{\rho^*} \frac{1}{\rho_{\rm cp}(L)}\frac{P(\rho^*,L)}{\rho^{*2}}\, d\rho^*.\end{aligned} \tag{22}$$

C. Kofke–Gibbs–Duhem integration

The location of a fluid–solid coexistence curve can be determined by performing several free-energy calculations and measurements of the equation-of-state for a large number of L/D values. However, this approach is computationally rather expensive. To avoid this problem, we use a modification of a method that was recently developed by Kofke to trace coexistence curves.[20] The advantage of this method is that only equation-of-state information *at the coexistence curve* is required to follow the L/D dependence of the melting curve. In its original form, the Kofke scheme is based on the Clapeyron equation which describes the temperature dependence of the pressure at which two phases coexist:

$$\frac{dP}{dT} = \frac{\Delta H}{T\Delta V}, \tag{23}$$

where ΔH is the molar enthalpy difference and ΔV the molar volume difference of the two phases. This equation is not self-starting, in the sense that one point on the coexistence

curve must be known before the rest of the curve can be computed by integration of Eq. (23). Kofke refers to this method as ''Gibbs–Duhem'' integration.

In the present case, we are not interested in the temperature dependence of the coexistence curve (this dependence is trivial for hard-core systems), but in the dependence of the coexistence pressure on L/D, the shape anisotropy of the spherocylinders. In order to obtain a Clapeyron-like equation relating the coexistence pressure to L/D, we should first write down the explicit dependence of the (Gibbs) free energy of the system on L/D:

$$dG = N\mu = VdP + \kappa dL, \tag{24}$$

where κ is the derivative $(\partial F/\partial L)_\rho$ defined in Eq. (20) and where we have used the fact that D is our unit of length. Along the coexistence curve, the difference in chemical potential of the two phases is always equal to zero. Hence,

$$\Delta\mu = \Delta v\, dP + \frac{1}{N}\Delta\kappa dL = 0, \tag{25}$$

where Δv is the difference in molar volume of the two phases at coexistence and $\Delta\kappa = \kappa_1 - \kappa_2$. From Eq. (25) we can immediately deduce the equivalent of the Clausius–Clapeyron equation

$$\frac{dP}{dL} = -\frac{1}{N}\frac{\Delta\kappa}{\Delta v}. \tag{26}$$

Kofke used a predictor-corrector scheme to integrate Eq. (23). However, we find that this integration scheme, when applied to Eq. (26), is not very stable. In particular, when the predicted pressure is slightly off, the predictor-corrector scheme leads to unphysical oscillations. We therefore introduce a slightly different integration procedure. Instead of calculating one new point in the phase diagram every step, we start with a set of simulations at different L values and pressure for both phases. The derivatives are calculated according to Eq. (26) and subsequently fitted to a polynomial in L

$$\frac{dP}{dL} = \sum_{i=0}^{3} \alpha_i L^i. \tag{27}$$

This polynomial is integrated to give new pressures which are used in the next iteration. The old and new pressures are mixed together to improve the stability. This procedure is repeated until convergence of the pressure has occurred. The set of starting values are obtained by application of the original Gibbs–Duhem scheme.

In Kofke's application of the Gibbs–Duhem method, the MC simulations are carried out in the isothermal-isobaric (NPT) ensemble. However, in the present case (hard-core particles), it is more efficient to use molecular dynamics to compute the derivative κ. In practice, we use a hybrid approach where MD simulations are embedded in a constant NPT-MC scheme. True constant-pressure MD is not an attractive option for hard-core models.

IV. PHASE DIAGRAM FOR $L/D \leqslant 5$

A. Phase behavior for $0 \leqslant L/D \leqslant 3$

For hard spherocylinders with lengths shorter than $L/D = 3$, there is only a fluid phase and, at high densities, a crystalline phase. For rods with $L/D \geqslant 0.35$, the crystalline phase is an orientationally ordered (hexagonal) lattice. Below $L/D = 0.35$ we find that a face-centered cubic ''rotator'' phase becomes stable (see Sec. V).

Gibbs–Duhem simulations were performed to locate transition from isotropic fluid to the fcc plastic crystal in the range $L/D = 0$–0.3. As a reference point, we used the coexistence properties of the hard-sphere model ($L/D = 0$).[26] In the region $0.4 \leqslant L/D \leqslant 3$, we used the free- energy data of Ref. 9 at $L/D = 1$ as our fixed reference point. As a test, we checked that the computed coexistence curve did reproduce results of Ref. 9 for the densities of the coexisting phases for $L/D = 3$.

The results of the Gibbs–Duhem integration are given in Table II and are displayed in Fig. 1. The coexistence curves are smooth and the densities reproduce the earlier values for $L/D = 3$ to within a few tenth of a percent. The solid density at $L/D = 2.4$ is slightly off, presumably because the solid happened to contain a defect. In any event, as $\Delta\kappa$ [in Eq. 26)] is evaluated as the (small) difference between two large, fluctuating numbers, it is difficult to obtain this quantity with high accuracy. An additional problem is that it takes a long time before the simulation box for the solid phase has relaxed to its equilibrium shape (i.e., the one that makes the pressure tensor isotropic).

The Gibbs–Duhem integration results for the fluid-rotator transition for $0 < L/D < 0.3$ can be compared with Monte Carlo simulations of the fluid-plastic crystal coexistence in hard dumbbell systems, performed by Singer and Mumaugh[27] and by Vega *et al.*[28,29] Figure 3 shows the fluid-rotator coexistence region of the spherocylinders in combination with the results on dumbbells. As one would expect, the agreement is excellent because the spherocylinder hardly differ from dumbbells in this L/D region.

We found that the Gibbs–Duhem integration could not be used in the region between $L/D = 0.3$ and $L/D = 0.4$ where three phases (liquid, plastic solid, and ordered solid) compete. On the basis of available data, we estimate that the liquid–solid–solid triple point is located around $L/D = 0.35$ and $\rho^* = 0.75$.

B. Phase behavior for $3 \leqslant L/D \leqslant 5$

In Fig. 4 the equations of state for spherocylinders with $L/D = 3$ to 5 are displayed. The reduced pressure is defined as $P^* = Pv_0/kT$, where v_0 is the molecular volume of the particle $[v_0 = \pi(LD^2/4 + D^3/6)]$.

We found for $L/D = 3$ a mechanically stable isotropic, smectic, and solid phase which is in agreement with the results of Veerman and Frenkel. For $L/D = 5$ we find also a mechanically stable nematic phase as was reported by Frenkel, Lekkerkerker, and Stroobants.[8] At values of L/D smaller than 5, the nematic phase region becomes narrower until it

TABLE II. Pressure and reduced densities of coexisting isotropic and solid phases for hard spherocylinders with shape anisotropies L/D between 0 and 3 as obtained by Gibbs–Duhem integration. The pressure is given in units of kT. The horizontal lines separate the results of independent integrations. The stars indicate the reference L/D values.

L/D	P/kT	ρ^*_{solid}	ρ^*_{iso}
0.00*	11.69	0.736	0.667
0.03	11.45	0.730	0.660
0.05	11.24	0.731	0.6600
0.07	11.05	0.725	0.661
0.10	10.91	0.723	0.695
0.12	10.83	0.719	0.658
0.15	10.83	0.715	0.659
0.17	10.93	0.715	0.661
0.20	11.14	0.713	0.666
0.23	11.49	0.714	0.670
0.25	11.98	0.717	0.679
0.28	12.63	0.719	0.686
0.30	13.46	0.724	0.696
0.40	21.94	0.821	0.766
0.50	20.06	0.821	0.753
0.60	18.24	0.819	0.745
0.70	16.51	0.814	0.733
0.80	14.89	0.809	0.720
0.90	13.41	0.801	0.711
1.00*	12.09	0.794	0.698
1.20	10.12	0.781	0.680
1.00*	12.08	0.792	0.697
1.20	10.19	0.781	0.679
1.40	8.64	0.767	0.662
1.60	7.39	0.756	0.647
1.80	6.41	0.743	0.634
2.00	5.64	0.732	0.620
2.20	5.03	0.724	0.619
2.40	4.56	0.706	0.602
2.60	4.17	0.710	0.601
2.80	3.81	0.702	0.589
3.00	3.45	0.691	0.588

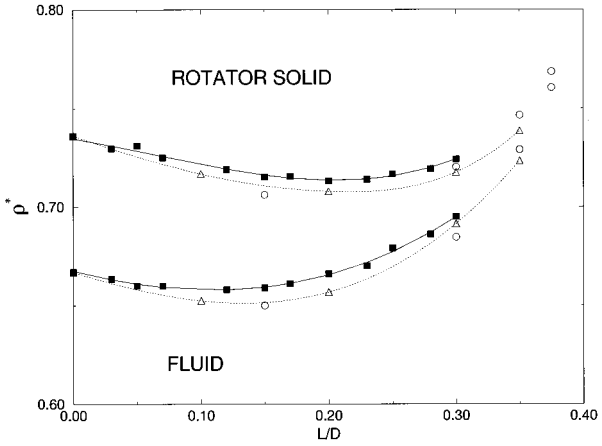

FIG. 3. Comparison between the Gibbs–Duhem integration results (squares) for the fluid-rotator transition of spherocylinders of length $L/D<0.3$ and the Monte Carlo simulation results of Singer and Mumaugh (triangles) (Ref. 27) and of Vega *et al.* (circles) (Ref. 29) for dumbbells of small L/D. The densities of the dumbbell phases are reduced in the same way as the densities of the spherocylinders. The lines through the points are a guide to the eye.

disappears when at $L/D\approx 3.7$ the isotropic-nematic-smectic triple point is reached.

Although the isotropic-nematic transition is a first order transition, the density jump and the hysteresis are too small to be observed in the simulations, at least for small L/D. Only for large values of L/D is the density gap sufficiently large to be observable in our simulations (see Sec. VI). We therefore estimated the location of the isotropic-nematic transition for $L/D<5$ by measuring the orientational correlation function

$$g_2(r)\equiv\langle P_2(\mathbf{u}(0)\mathbf{u}(r)\rangle, \tag{28}$$

where P_2 is the second Legendre polynomial and $\mathbf{u}(0)$ is the unit vector characterizing the orientation of a particle at the origin while $\mathbf{u}(r)$ denotes the orientation of a particle at a distance r from the origin. The brackets indicate ensemble averaging.

$g_2(r)$ becomes long ranged at the isotropic-nematic transition and its limiting value at large r tends to S^2, where S is the nematic order parameter. Of course, in a periodic system, it is not meaningful to study correlations at distances larger than half the box length, $B/2$. Figure 5 shows that half the box length is indeed sufficient to reach the limiting behavior of $g_2(r)$. In Fig. 6 we have plotted the density dependence of the nematic order parameter estimated from the value of $g_2(r=B/2)$. At the isotropic-nematic transition there is a steep increase of S. We estimate the transition to take place at an order parameter $S=0.4$. The transition densities are summarized in Table III.

In our simulation studies we could distinguish the isotropic phase from the nematic by looking at the nematic order parameter S. The smectic phase is characterized by a density modulation along the director. At the same time the pair correlation function in one smectic layer in the transverse direction is still fluidlike. The difference between the smectic and crystalline phases is that the crystal also shows transverse ordering in the density. Details on the identification of the phases can be found in Ref. 9.

Inspection of the equation of state suggests that the nematic-to-smectic phase transition is almost continuous at $L/D=5$, but becomes clearly first order for smaller values of L/D. A first order smectic-to-solid transition is found for $L/D>3.1$, as can be seen in Fig. 4. In order to locate the coexistence curves we used thermodynamic integration as described in Sec. III B to compute the absolute free energy of the smectic and solid phase and the free-energy difference between a smectic and a nematic. The resulting values are displayed in, respectively, Tables IV, V, and VI. Combination of these free energies with the equation of state and subsequent application of the double tangent construction leads to the coexisting densities of the nematic to smectic transition, the smectic-solid transition as well as the (metastable) solid to isotropic-liquid transition at $L/D<3.7$. The results have been summarized in Table VII.

The isotropic-smectic-solid triple point is located at $L/D=3.1$. The smectic phase is thermodynamically stable at higher L/D and is separated from the solid and the isotropic liquid by coexistence regions. The I-SmA-S triple point oc-

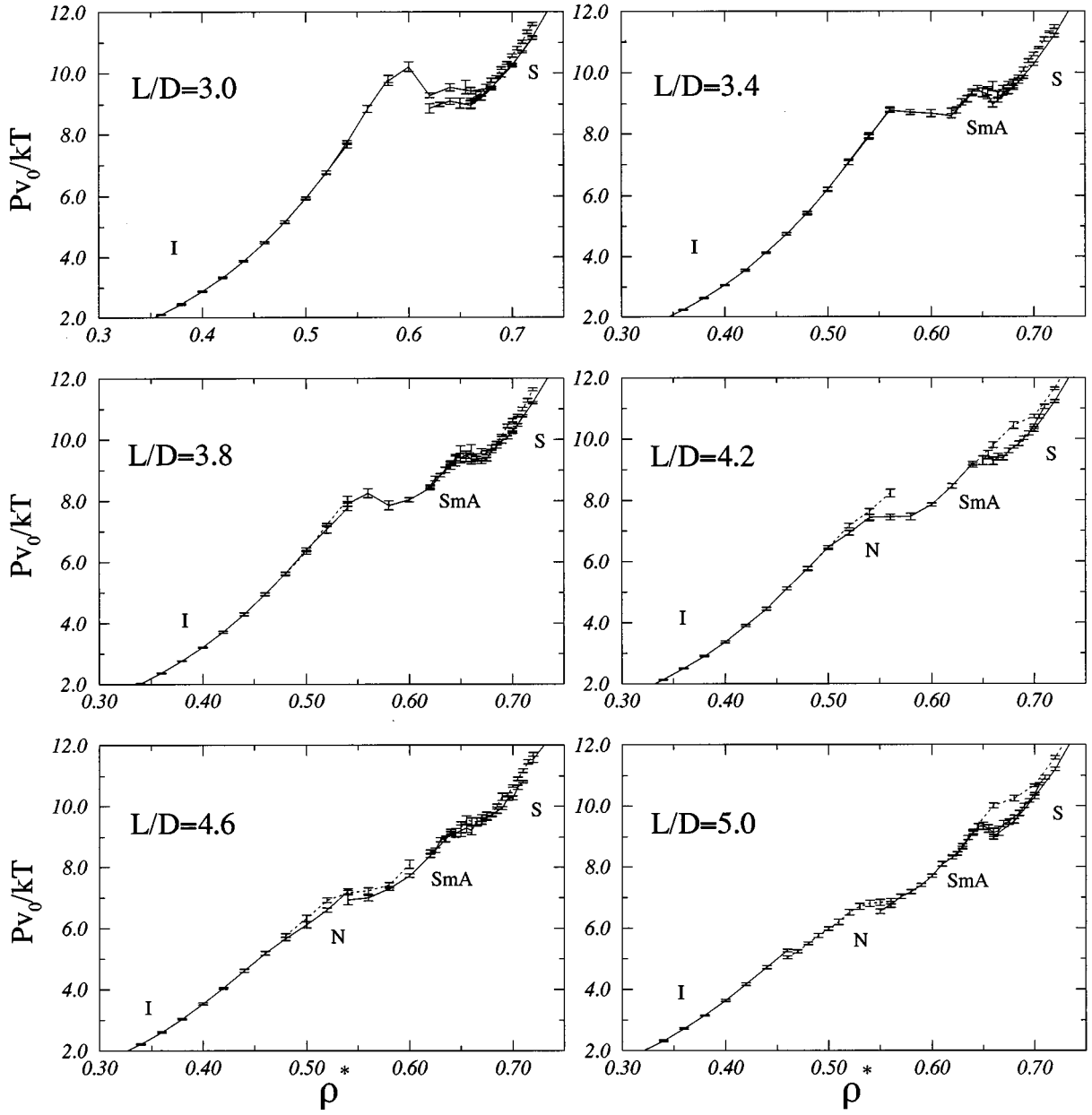

FIG. 4. Equations of state for spherocylinders with shape anisotropy L/D between 3 and 5. The pressure is expressed in the dimensionless unit Pv_0/kT, where v_0 is the molecular volume of the spherocylinders. The dashed curves correspond to a compression whereas the solid curves denote an expansion. The different mechanically stable phases are indicated.

curs at a smaller L/D value then the I-N-SmA triple point. This is not surprising as the smectic phase is already found to be mechanically stable at $L/D=3$, whereas the nematic phase is not.

In their study of the phase diagram of spherocylinders with $L/D=3$ to $L/D=5$, McGrother *et al.*[15] estimated the isotropic-smectic-solid triple point to occur at $L/D=3.2$, followed by an isotropic-nematic-smectic point at $L/D=4$. The small disagreement between these numbers and our results may be due to the fact that their estimates are based on equations of state obtained by NPT Monte Carlo simulation of spherocylinders in a cubic box. It is known that the pressure of a smectic can become anisotropic in a cubic box, resulting in an increase of the free energy. Moreover, the free-energy calculation method used here is in principle a more reliable method to obtain the phase boundary than examination of the equation of state. Yet, it should be stressed that a small error in the free energy will have a noticeable effect on the estimate of the phase boundaries.

The nematic-to-smectic phase transition appears to be first order even for $L/D>5$. This is rather surprising as in previous simulations this nematic-smectic transition appeared to be continuous.[9] However, McGrother *et al.*[15] also found the nematic-smectic transition at $L/D=5$ to be first order, albeit with coexistence densities and pressures that are slightly different from ours. This minor difference is prob-

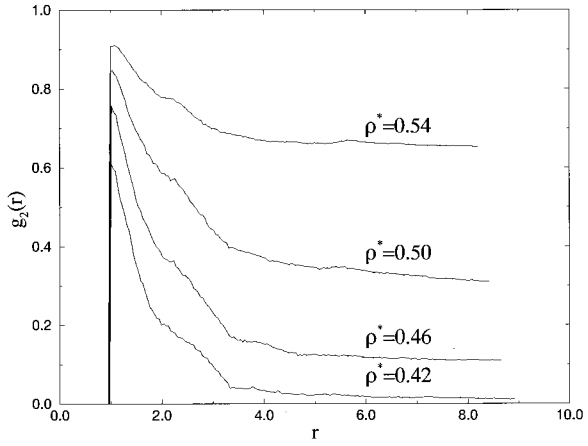

FIG. 5. Orientational correlation function $g_2(r)$ [see text, Eq. (28)] at different densities for $L/D=4.6$. The figure shows that $g_2(r)$ reaches a constant value for $r=B/2$.

ably due to the fact that McGrother *et al.* did not use free-energy calculations to locate the coexistence curves.

The reduced densities of the coexisting smectic and solid phases are $\rho^*\approx 0.66$ and $\rho^*\approx 0.68$, respectively. These densities depend only weakly on L/D and are effectively constant for L/D larger than 5. As the smectic-solid transition is closely related to the freezing of the quasi-two-dimensional liquid layers, it is interesting to compare the density where this transition takes place with the freezing density of hard disks. The quasi-2D in-layer density for the coexisting smectic and solid phases are $\rho_{2D,l}=0.789$ and $\rho_{2D,s}=0.83$, respectively. This should be compared to the most recent estimates of the solid–liquid coexistence of hard disks:[30] $\rho_{\mathrm{liq}}=0.887$ and $\rho_{\mathrm{sol}}=0.904$.

TABLE III. Pressure and reduced density of the isotropic to nematic transition for hard spherocylinders with shape anisotropies L/D between 3 and 5. The pressure is expressed in dimensionless units Pv_0/kT, where v_0 is the molecular volume of the spherocylinders.

L/D	Pv_0/kT	ρ^*
3.40	9.58	0.58
3.80	7.23	0.54
4.20	6.36	0.52
4.60	5.48	0.48
5.00	4.97	0.45

V. THE ROTATOR PHASE

A. Finite densities

A hexagonal crystal consisting of long rods will have a high orientational correlation as all rods are, on average, aligned. On the other hand, a solid of short spherocylinders will behave almost like a hard-sphere solid. In particular, the orientational distribution function will have cubic symmetry, approaching an isotropic distribution in the limit $L/D\rightarrow 0$.

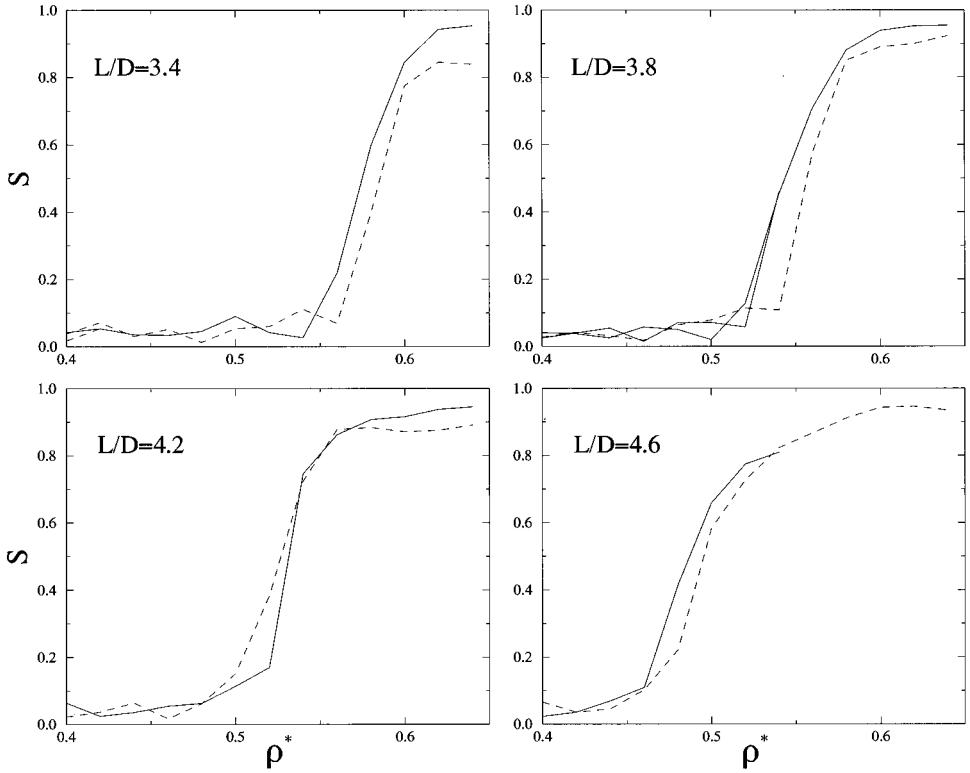

FIG. 6. Density dependence of the nematic order parameter, as estimated from the limiting behavior of the orientational correlation function $g_2(r)$ (see text) for hard spherocylinders with L/D between 3.4 and 4.6. The solid curve corresponds to an expansion branch, the dashed curve to a compression branch.

TABLE IV. Free energy and contributions to the free energy of the smectic phase. Columns 5 to 10 in the table refer to terms in the rhs of Eq. (15). The maximum values of μ and λ were $\mu_0=1000$ and $\lambda_0=10\,000$. The number of particles in the system was 540.

Phase	L/D	ρ^*	ρ_{disk}	$\beta F^{\mathrm{ex}}_{\mathrm{disk}}/N$	$\beta F^{p,\mathrm{id}}_{\lambda_0,\mu_0}/N$	$\ln V/N$	$\int\langle\Delta r^2\rangle$	$\int\langle\sin^2\theta\rangle$	$\int\langle\Delta\ \sin^2\theta\rangle$	$\beta F_{\lambda,\mu=0}/N$
SmA	3.0	0.64	0.789	1.430	10.254	0.0146	2.364	4.232	−0.005	5.079
SmA	5.0	0.66	0.810	1.624	10.254	0.0154	2.592	3.206	−0.277	6.341
SmA	5.0	0.68	0.841	1.941	10.254	0.0153	2.684	2.943	−0.312	6.864

The orientationally ordered solid should (according to Landau theory[31]) be separated from the plastic solid by a first order phase transition.

Usually, it is assumed that hard spheres form an fcc crystal structure. Near melting, it is known that the difference in stability of the fcc and hcp structures is very small.[25] In our simulations in the close-packed limit (see the next section) we found that the free-energy difference between both crystal structures at close packing is less than 10^{-3} kT. In what follows, we will assume for the sake of convenience that the stable solid structure is fcc, for hard spheres as well as spherocylinder systems.

We estimated the coexistence region between the aligned and rotator solids by measuring the equation of state for lengths $L/D=0.01$, 0.1, 0.2, and 0.3 at high densities combined with free-energy calculations at these lengths. The equations of state were measured in MD simulations, as described in Sec. III A and are shown in Fig. 7. The free energy of the aligned solid was calculated using thermodynamic integration as describes in Sec. III B 2. For the rotator phase, we found it more convenient to relate the free energy to that of a hard-sphere reference system. At a given density ρ, the free energy for a plastic crystal of rods with length L is given by Eq. (22):

$$\frac{F(\rho,L)}{N}=\frac{F_{\mathrm{HS}}(\rho,0)}{N}+\int_0^L\kappa(\rho,L')dL'. \tag{29}$$

If we keep the reduced density constant, this changes into

$$\frac{F(\rho^*,L)}{N}=\frac{F_{\mathrm{HS}}(\rho^*,0)}{N}+\int_0^L dL'\left(\kappa(\rho^*,L')-\frac{\sqrt{3}}{2\rho^*}P(\rho^*,L')\right). \tag{30}$$

The free energy of the three-dimensional hard-sphere solid F_{HS} is well known and can be accurately represented using the analytical form for the equation of state proposed by Hall[32] in combination with a reference free energy of a fcc crystal obtained by Frenkel and Ladd.[25] The equations of state are displayed in Fig. 7 and the results of the free-energy calculation are given in Table VIII. Applying the double tangent construction results in Table IX. It is clear that in the limit $L/D\to 0$ the plastic-ordered coexistence curve terminates at the density of regular close packing. As can be seen from Fig. 8, the densities of the coexisting solid phases appear to depend almost linearly on L/D. The solid curve in Fig. 8 is an estimate for the solid–solid coexistence curve obtained by extrapolation of the simulation data *at close packing*. The simulation technique used to study this limit will be discussed below.

B. Close-packing limit

The rotator solid transition is expected to be first order even in the limit $\rho^*\to 1$ and $L/D\to 0$. We cannot access this region using ordinary simulation methods. However, somewhat surprisingly, it is possible to perform a simulation in this limit and get useful information about the limiting behavior of the solid–solid transition.

To see how this is achieved, let us first consider the case where $\rho-\rho_{\mathrm{cp}}$ and L/D are both small but finite. In the dense solid phase, the particles are constrained to move in the vicinity of their lattice positions and we can safely ignore diffusion. Therefore, we only have to take the deviations from the lattice positions into account. The overlap criterion of two spherocylinders i and j is based on the shortest distance between the two cylinder axes with orientation $\mathbf{u_i}$ and $\mathbf{u_j}$ (see Ref. 12),

$$\mathbf{r}_{ij}=\mathbf{r}^{\mathrm{cm}}_{ij}+\alpha\mathbf{u_i}-\beta\mathbf{u_j}, \tag{31}$$

where $\mathbf{r}_{ij}$ is the shortest distance vector, $\mathbf{r}^{\mathrm{cm}}_{ij}$ is the center-of-mass separation of neighboring particles j, and α and β are the distances along the axis of the two particles from the center-of-mass to the point of closest approach. In a dense solid, we can rewrite the center-of-mass separation as the vector sum of $\mathbf{r}^0_{ij}$, the distance between the lattice positions of i and j, and $\mathbf{\Delta}_{ij}$, the difference of the vector displacements of particles i and j from their lattice positions. Hence,

TABLE V. Free energy and contributions to the free energy of the solid phase. Columns 6 to 9 in the table refer to terms in the rhs of Eq. (4). The maximum values of μ and λ are displayed as well. The number of particles in the system was 540.

Phase	L/D	ρ^*	$\mu_{\max}$	$\lambda_{\max}$	$\beta F^{\mathrm{ein}}_{\lambda_0,\mu_0}/N$	$\ln V/N$	$\int\langle\Delta r^2\rangle$	$\int\langle\sin^2\theta\rangle$	$\beta F_{\lambda,\mu=0}/N$
S	3.0	0.82	22 025	22 025	21.438	0.014	7.529	3.812	10.082
S	5.0	0.76	20 000	20 000	21.197	0.015	8.708	3.587	8.886
S	5.0	0.86	50 000	50 000	23.485	0.015	8.138	3.194	12.140

TABLE VI. Contributions to the free-energy difference of a nematic phase at $\rho^*=0.5$ and a the smectic phase at $\rho^*=0.6$ for $L/D=4.5$. The different integrals in the table refer to terms in the rhs of Eq. (17). The maximum value of λ was chosen to be 5. The number of particles in the system was 600.

$\int\langle\cos\rangle_{\rho^*=0.6}$	$\int_{0.5}^{0.6}P(\rho)/\rho^2 d\rho^*$	$\int\langle\cos\rangle_{\rho^*=0.5}$	$\beta\Delta F_{\text{nem-smec}}/N$
0.2849	2.034	0.893	2.642 29

$$\mathbf{r}_{ij}=\mathbf{r}_{ij}^0+\mathbf{\Delta}_{ij}+\alpha\mathbf{u_i}-\beta\mathbf{u_j}. \tag{32}$$

It is important to realize that, in the limit $L/D\to 0$, all spherocylinder contacts will involve only the spherical end caps. Moreover, near close packing, the relative particle displacements Δ_{ij} will become negligible compared to the lattice vectors $\mathbf{r}_{ij}^0$. In this limit, the vector distance of closest approach between two spherocylinders will therefore be parallel to the lattice vector $\mathbf{r}_{ij}^0$. We need therefore only consider the component of $\mathbf{r}_{ij}$ along the direction of $\mathbf{r}_{ij}^0$.

It is most convenient to express the lattice vectors $\mathbf{r}_{ij}^0$ in terms of the unit vectors $\hat{\mathbf{b}}_{ij}$ that denote the directions of nearest neighbor bonds in the undistorted fcc lattice. In that lattice, the lattice vector $\mathbf{r}_{ij}^0$ can be written as

$$\mathbf{r}_{ij}^0(\text{fcc})=D\hat{\mathbf{b}}_{ij}.$$

In the close-packed spherocylinder crystal, the lattice is expanded along the [111] axis by an amount $1+(L/D)\sqrt{3/2}$. If we consider a crystal near (but not at) close packing, the crystal will expand in all three directions, but not necessarily isotropically. We assume that this expansion does not change the symmetry of the lattice—i.e., if we define the alignment direction of the spherocylinders (the [111] direction) to be the z axis, then we assume that the expanded crystal can be generated from the close-packed crystal by isotropic expan-

TABLE VII. Pressure, densities, and nematic order parameters of coexisting isotropic, nematic, and solid phases for hard spherocylinders with shape anisotropies L/D between 3 and 5. Units as in Table III. The order parameters are taken directly from the simulation results, without any interpolation.

Type of transition	L/D	Pv_0/kT	ρ_1^*	ρ_2^*	S_1	S_2
isotropic	3.0	10.23	0.587	0.663	0.06	0.95
(nematic)	3.2	9.56	0.576	0.647	-	-
-smectic	3.4	9.00	0.567	0.631	0.04	0.93
	3.6	8.54	0.559	0.616	-	-
	3.8	8.13	0.552	0.602	0.70	0.90
	4.0	7.77	0.545	0.590	-	-
	4.2	7.44	0.538	0.579	0.74	0.89
	4.4	7.10	0.532	0.571	-	-
	4.6	6.84	0.525	0.562	0.76	0.90
	4.8	6.60	0.519	0.553	-	-
	5.0	6.40	0.513	0.546	0.74	0.90
smectic	3.0	9.736	0.650	0.685	0.93	0.972
solid	3.4	9.830	0.655	0.686	0.96	0.981
	3.8	9.903	0.659	0.687	0.97	0.989
	4.2	10.009	0.663	0.689	0.97	0.991
	4.6	10.187	0.666	0.693	0.97	0.992
	5.0	10.428	0.669	0.699	0.98	0.994

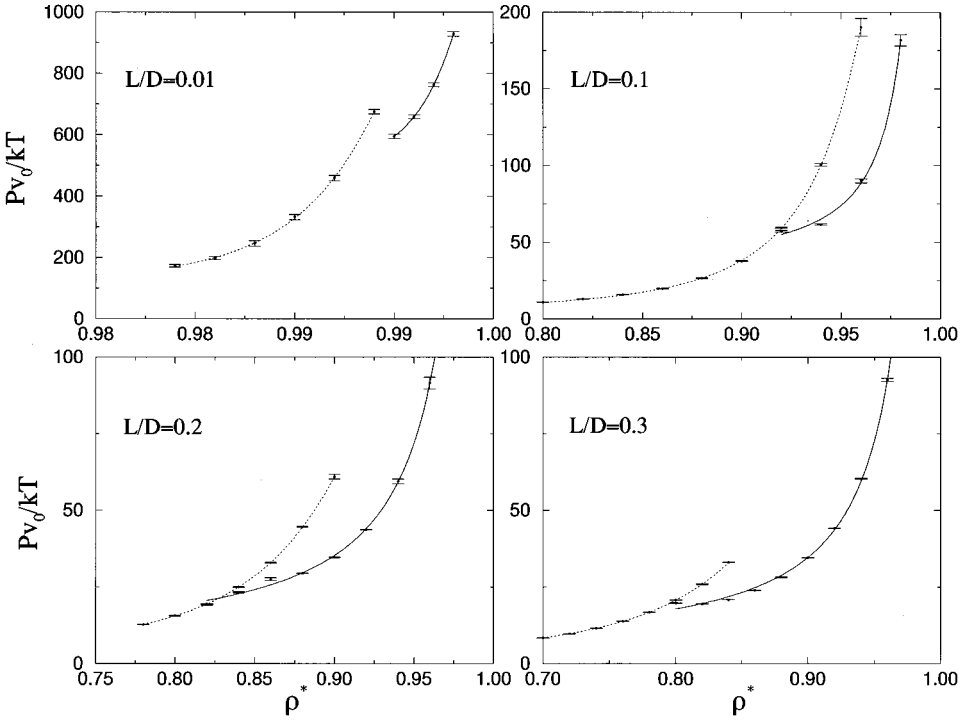

FIG. 7. Equations of state of the solid phases for L/D = 0.01, 0.1, 0.2, and 0.3. The dotted curve was obtained by compression and the solid curve by expansion. The strong hysteresis is indicative of a first order phase transition between the orientationally ordered solid and the rotator phase.

TABLE VIII. Helmholtz free energy per particle for plastic and orientationally ordered phases with L/D between 0.01 and 0.3. The free energies are expressed in units of kT.

L/D	ρ^*_{plastic}	βF_{plastic}	ρ^*_{ordered}	βF_{ordered}
0.01	0.982	12.01	0.9959	20.422
0.10	0.8	3.918 89	0.96	13.11
0.20	0.8	4.706 62	0.9	9.529 29
0.30	0.8	5.7323	0.9	10.1827

sion in the xy plane plus a (different) expansion along the z axis. It is convenient to express the lattice vectors of the expanded lattice as follows

$$\mathbf{r}^0_{ij}=(b_{x,ij}(D+a_x),b_{y,ij}(D+a_y),b_{z,ij}(D+a_z+L\sqrt{3/2}). \tag{33}$$

Note that, as we consider the limit $L/D\to 0$ and $\rho^*\to 1$, L and a_x, a_y, a_z are much smaller than D. Because of the assumed symmetry in the xy plane, $a_x=a_y\equiv a_{xy}$. We denote the average value of a_x, a_y, and a_z by a. It is related to the expansion of the lattice

$$a\equiv\frac{2a_{xy}+a_z}{3D}=(\rho^*)^{-1/3}-1. \tag{34}$$

If we define $\Delta\mathbf{u}_{ij}=\alpha\mathbf{u_i}-\beta\mathbf{u_j}$, the absolute shortest distance becomes

$$r^s_{ij}=\mathbf{r}_{ij}\cdot\hat{\mathbf{b}}_{ij}=D+a_{xy}+b^2_{z,ij}(a_z+L\sqrt{3/2}-a_{xy}) + \hat{\mathbf{b}}_{ij}.(\mathbf{\Delta}_{ij}+\Delta\mathbf{u}_{ij}). \tag{35}$$

As the spherocylinders can only touch with their spherical end caps, the surface-to-surface distance is given by

$$s_{ij}\equiv r^s_{ij}-D=a_{xy}+b^2_{z,ij}(a_z+L\sqrt{3/2}-a_{xy})+\hat{\mathbf{b}}_{ij}\cdot\mathbf{\Delta}_{ij} \tag{36}$$

$$+L/2(|\hat{\mathbf{b}}_{ij}.\Delta\mathbf{u}_i|+|\hat{\mathbf{b}}_{ij}.\Delta\mathbf{u}_j|), \tag{37}$$

where, in the last line, we have used the values for α and β appropriate for the distance between spherical end caps. The spherocylinder overlap criterion in the limit $a\to 0$, $L/D\to 0$ is simply

$$s_{ij}<0.$$

It turns out to be more convenient to express all distances in units of a. The density enters the problem through $x\equiv L/a$. We can now perform a Monte Carlo simulation of this model by setting up an undistorted fcc lattice with unit nearest neighbor distances, and move a randomly selected spherocylinder i from its initial scaled displacement Δ_i and orientation u_i to a trial displacement and orientation in such a way that microscopic reversibility is satisfied. We use the conventional Metropolis rule to accept or reject the trial move.

TABLE IX. Pressure and reduced densities of coexisting plastic and orientationally ordered solid phases for hard spherocylinders with shape anisotropies L/D between 0 and 0.3. Units as in Table III.

L/D	Pv_0/kT	ρ^*_{rot}	ρ^*_{aligned}
0	∞	1	1
0.01	1304.52	0.9921	0.994 33
0.1	107.71	0.9237	0.9393
0.2	49.99	0.862	0.896
0.3	29.91	0.808	0.845

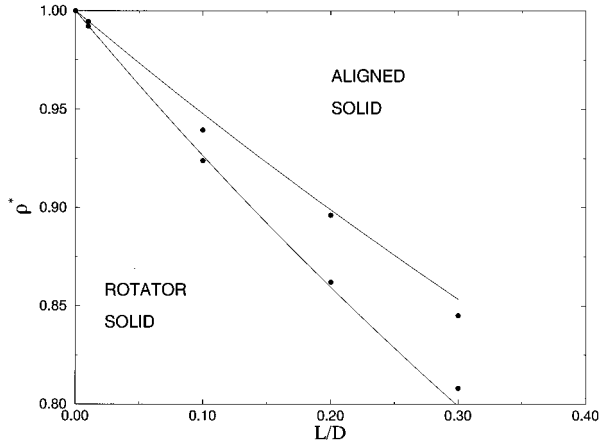

FIG. 8. Coexistence curves for the plastic solid orientationally ordered solid transition. The filled circles indicate the coexistence densities obtained by off-lattice simulations. The solid lines are the close-packing limit results discussed in Sec. V B.

The system is anisotropic and we must allow box shape fluctuations to ensure equilibrium. In the simulation the box shape is determined by the ratio of a_{xy} and a_z. During trial moves that change the shape of the simulation box, the total volume should stay constant. Equation (34) then implies that the changes in a_{xy} and a_z are related by

$$2\Delta a_{xy}=-\Delta a_z. \tag{38}$$

The conventional Metropolis criterion is used to decide on the acceptance of shape-changing trial moves. To speed up equilibration, we also used molecular dynamics simulations of the close-packed spherocylinder model. The MD scheme that we use is essentially identical to the one used in off-lattice simulations.[23,24] All the distances are scaled with a factor a. In the scaled space the new overlap criterion of Eq. (36) is used to locate colliding pairs. The virial expression for the pressure in the close-packing limit is

$$\frac{\beta P}{\rho}-1=\frac{1+a}{3aN}\sum_{i<j}\langle\mathbf{f}_{ij}\cdot\hat{\mathbf{b}}_{ij}\rangle\equiv\frac{1+a}{a}z(\rho), \tag{39}$$

where $\mathbf{f}_{ij}$ denotes the rate of momentum transfer between spherocylinders i and j, and the last line defines the quantity $z(\rho)$ that is measured in the simulations. Simulations were performed both by compression from ''low'' density (i.e., low L/a) and by expansion from ''high'' density (high L/a). The free energy of both the rotator and the aligned phases were calculated by Einstein integration as discussed in the previous chapter. It should be noted that the free energies of both phases do in fact diverge at close packing. However, the free-energy *difference* is finite, and this is what we need to compute the phase coexistence.

In order to see how this can be achieved, consider the expression for the free energy of a (fixed center-of-mass) Einstein crystal in the limit of close packing. Every particle in the hard-spherocylinder crystal is confined to move within a cell with average radius a. We wish to switch on an Einstein spring constant that is sufficiently large to suppress hard-core overlaps. This can only be achieved if the spring-constant $\lambda_{\max,1}$ in 5 is of order $1/a^2$. Hence, we expect $\lambda_{\max,1}a^2$ to be finite. It is therefore convenient to write the free energy of the Einstein crystal as follows

$$\beta F_{\rm ein}=\frac{3}{2}\ln N-\frac{3}{2}(N-1)\ln\frac{\pi}{\lambda_{1,\rm sc}}-N\ln\frac{2\pi}{\lambda_2}-3(N-1)\ln a, \tag{40}$$

where we have defined $\lambda_{1,\rm sc}$ as $a^2\lambda_1$. Note that λ_2, the ''orientational'' spring constant remains finite. The expression for the free energy of the spherocylinder crystal [Eq. (4)] now becomes

$$\frac{\beta F(L/a)}{N}+\frac{3(N-1)}{N}\ln a=\frac{3}{2N}\ln N-\frac{3}{2}(N-1)\ln\frac{\pi}{\lambda_{\max,\rm sc}}-N\ln\frac{2\pi}{\lambda_{\max,2}}-\frac{\ln V}{N}-\int_0^{\lambda_{\max,\rm sc}}d\lambda_{\rm sc}\left\langle\frac{\Delta r^2}{a^2}\right\rangle_{\lambda_{\rm sc}}-\int_0^{\lambda_{\max,2}}d\lambda_2\langle\sin^2\theta\rangle_{\lambda_2}. \tag{41}$$

The computational scheme is essentially the same as with the conventional Einstein crystal method. The main difference is that all displacements in Eq. (41) are expressed in units of a. The scaled coupling constant $\lambda_{\max,\rm sc}$ remains finite. All divergences are now contained in the $3(N-1)/N\ln a$ term. When searching for the point of phase coexistence, we need to be able to compute the variation of the free energy with density. The free energy at any value of $x=L/a$ is obtained by thermodynamic integration starting from the density ρ_0 where the direct free-energy calculation has been performed

$$\frac{\beta F(\rho)}{N}=\frac{\beta F(\rho_0)}{N}+\int_{\rho_0}^{\rho}\frac{\beta P(\rho')}{\rho'^2}\,d\rho'. \tag{42}$$

It is more convenient to change to the integration variable $x\equiv L/a$, which is related to the density through $x=L/(\rho^{*-1/3}-1)$. In the MD simulations we do not measure the pressure $P(x)$ but rather $z(x)$ [see Eq. (39)]. The variation of the Helmholtz free energy with x can be written as

$$\beta F(x)/N=\beta F(x_0)/N+3\int_{x_0}^{x}\frac{z(x')}{x'}\,dx'. \tag{43}$$

At coexistence the pressure in both phases is equal. Using Eq. (39) and $x\equiv L/a$, it is straightforward to show that the condition $P_1=P_2$ can be written as

$$\frac{1+(x_1/L)z(x_1)(1+L/x_1)}{(1+L/x_1)^3}=\frac{1+(x_2/L)z(x_2)(1+L/x_2)}{(1+L/x_2)^3}.$$

To leading order in $1/L$ this implies that

$$x_1z(x_1)=x_2z(x_2). \tag{44}$$

The chemical potential is given by

$$\beta\mu(x)=\beta F(x)/N+\frac{\beta P(x)}{\rho}. \tag{45}$$

The condition for equilibrium, $\mu_1=\mu_2$, corresponds to

$$\beta F(x_1)/N+\beta\rho_0P(x_1)(1+L/x_1)^3=\beta F(x_2)/N+\beta\rho_0P(x_2)(1+L/x_2)^3. \tag{46}$$

All terms in this equation diverge in the close-packing limit. However, all differences remain finite. This is immediately obvious for the terms involving the pressure as, at coexistence, $P(x_1)=P(x_2)$. We recall that the free energy diverges as

$$-3\frac{N-1}{N}\ln a=-3\frac{N-1}{N}(\ln L-\ln x).$$

We can therefore write the Helmholtz free energy of the crystal as a nondiverging part $F_r(x)$, where the subscript r stands for *regular*, and the diverging remainder

$$\beta F(x)/N\equiv\beta F_r(x)/N-3\frac{N-1}{N}(\ln L-\ln x).$$

The condition for the equality of the chemical potential now becomes

$$\beta F_r(x_1)/N+3\frac{N-1}{N}\ln x_1+3z(x_1)=\beta F_r(x_2)/N+3\frac{N-1}{N}\ln x_2+3z(x_2), \tag{47}$$

where we have dropped the terms that cancel on the left- and right-hand side and where we have ignored terms that vanish in the limit $a\to0$.

Figure 9 shows the ''equation of state'' $xz(x)$ for the

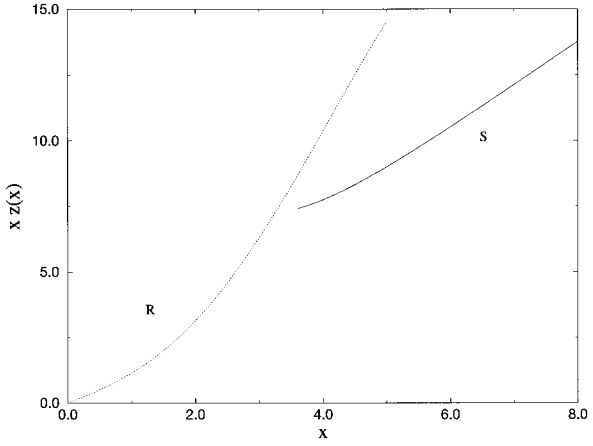

FIG. 9. Scaled equations of state for hard spherocylinder solids in the limit $a\to0,L\to0$ [see Eq. (44)]. The dotted curve denotes a compression and the solid curve corresponds to an expansion.

dense plastic crystal and ordered solid. The free energies of the reference systems are given in Table X. The coexistence values of x, pressure, and chemical potential that follow from Eqs. (44) and (47) are

$$x_{\mathrm{rot}} = 3.863\ 17,$$
$$x_{\mathrm{sol}} = 5.525\ 43,$$
$$xz(x) = 9.778\ 35,$$
$$\beta\mu_r = 10.7092, \tag{48}$$

where μ_r is the regular part of the chemical potential, given by Eq. (47). As x is defined as the ratio of L and a, Eq. (48) describes the initial (small L) dependence of the plastic-ordered transition on the spherocylinder length. As presented, a given value of x corresponds to a slope of the coexistence curve in the $\{L,a\}$ plane. However, by using the definition of x,

$$\rho^* = \frac{1}{\left(\frac{L}{x}+1\right)^3}, \tag{49}$$

every value of x corresponds to a curve in the $\{\rho^*,L\}$ plane. The resulting solid–solid coexistence curves are plotted in Fig. 8. It is interesting to note that, even at L/D as large as 0.3, the slope of rotator-solid coexistence curve is still dominated by the behavior at close packing.

VI. PHASE DIAGRAM IN THE $L/D = 5-60$ REGION

A. Numerical techniques

The numerical study of the spherocylinder phase diagram for systems of longer rods is not different in principle from the study for shorter rods. However, in practice, there are many differences. Almost all of these differences imply that simulations of longer rods are more time consuming. For one thing, the simulation of long rods requires large system sizes. The simulation box should be large enough to accommodate at least two rod lengths in order to avoid the situation that one particle can, at the same time, overlap with more than one periodic image of another particle. The number of particles required at a given density scales with L^3 whereas the number density at the I-N transition is expected to scale as $1/L^2$. In practice, it turns out that if we wish to impose the condition that the box diameter is larger than $2L$, then for $L/D=50$ at the isotropic-nematic transition, one needs at least 3000 particles. The disadvantage of using such a large number of particles is that the simulations become very slow and, as a consequence, the statistical accuracy tends to be poor. We therefore decided to work with somewhat smaller systems where multiple overlaps, although rare, are not completely excluded. Of course, this implies that we must now also test for overlap with more than one periodic image. The possibility of two simultaneous overlaps with the same particle is taken into account by doing three independent overlap tests. Usually, the pair overlap test routine selects a first particle, looks for the nearest periodic image of the second particle with respect to the first one, and calculates the shortest distance between the pair. There is an overlap if this distance is smaller than D. If the box is smaller than $2L$, more than one overlap is possible, but not more than two. Figure 10 illustrates this. In principle, particle A could overlap with B and its periodic images B' and B'', but it cannot overlap with any of the other periodic images at the same time provided the box length is larger than $L+2D$. For instance, A cannot overlap with B''' if the cylinder axis of A does not enter the periodic image of the box containing B'''. We devised an overlap routine which looks for the three images B, B', and B'' and check those for overlap in the usual way. This routine is applicable to both MD and MC, including Gibbs-ensemble MC. Although this routine seems more time consuming because it has to check for three overlaps instead of one, it is still preferable to perform an overlap test for several periodic images than to perform all simulations for a larger system.

In the region $L/D=15$–50 the isotropic-nematic transition was studied both by Gibbs-ensemble simulation[33,34] and Gibbs–Duhem integration.[20] We started with an $L/D=40$ isotropic random configuration at low density and a perfectly

TABLE X. Regular part of the Helmholtz free energy per particle in the close-packed limit. The values have been obtained by Einstein integration.

x	$\beta F_r(x)$
0.5	−3.800
1.0	−1.076
5.0	0.0394
6.0	0.400
7.3	0.833
12	1.908

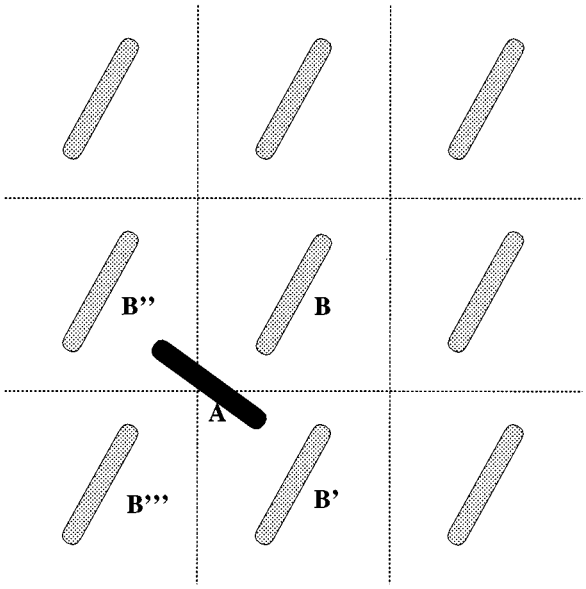

FIG. 10. Situation sketch in 2D for multiple overlap check. Particle A cannot overlap with a periodic image of B if the cylinder axis is outside a periodic image of the box, as indicated by the dotted lines. In principle, A could overlap with B, B′, and B″. These images have to be checked, whereas all others can be ignored.

TABLE XI. Pressure, densities, and nematic order parameters of coexisting isotropic and nematic phases for hard spherocylinders with shape anisotropies L/D between 15 and 50. The coexistence data in this table were obtained using the modified Gibbs–Duhem integration procedure described in the text. Units as in Table III.

L/D	Pv_0/kT	ρ_I^*	ρ_N^*	S_I	S_N
15.00	0.0970	0.1978	0.2291	0.041	0.784
20.00	0.0516	0.1548	0.1902	0.109	0.808
25.00	0.0322	0.1271	0.1565	0.076	0.806
30.00	0.0220	0.1044	0.1252	0.093	0.832
35.00	0.0159	0.0919	0.1101	0.094	0.818
40.00	0.0120	0.0819	0.1043	0.076	0.825
45.00	0.0093	0.0737	0.0840	0.102	0.840
50.00	0.0072	0.0673	0.0825	0.013	0.842

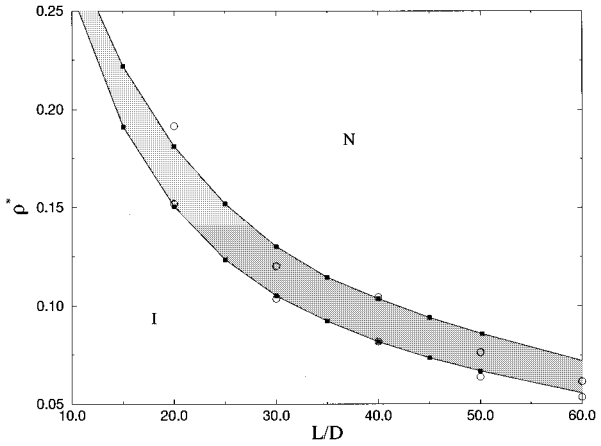

FIG. 11. Isotropic-nematic transition in a system of hard spherocylinders with shape anisotropy L/D between 15 and 60. The drawn curves have been obtained by modified Gibbs–Duhem integration. The open circles denote the results of Gibbs-ensemble simulations (see text).

aligned configuration at high density. Using Gibbs-ensemble MC these configurations were equilibrated to coexistence. This coexistence was used to perform a quick standard Gibbs–Duhem integration in the range $L/D=15$–50 to obtain an initial estimate for the coexistence curve. Subsequently, we used this set of configurations to start the ''parallel'' Gibbs–Duhem technique described in Sec. III C. This calculation was continued until the coexistence curve had fully converged. As a check, Gibbs-ensemble MC simulations were also performed for $L/D=20,\ 30,\ 50$, and 60.

B. Results

The results of the Gibbs–Duhem integration of the long rods are shown in Table XI and the coexistence densities are plotted in Fig. 11. The Gibbs ensemble results are displayed in Table XII. As can be seen, the results of both methods agree quite well.

In Fig. 12 we have replotted the phase diagram in a way that makes comparison with the Onsager limit easier. In particular, we now use as our density variable

$$c \equiv \rho B_2 = \frac{1}{4}\pi L^2 D \rho.$$

In these units the coexistence densities remain finite in the Onsager limit $L/D \to \infty$. In order to facilitate the extrapolation to the Onsager limit, we use D/L rather than L/D as the variable characterizing the aspect ratio of the rods. Figure 12 shows that the I-N coexistence curves extrapolate nicely to the Onsager limit at $c_{iso}=3.29$ and $c_{nem}=4.19$,[35] except for a few points on the nematic coexistence curve at high L/D. Apparently, at these high lengths it is difficult to equilibrate the nematic phase completely. It is clear from Fig. 12 that already for rods with a shape anisotropy less than $L/D=20$ (or $D/L>0.05$), the Onsager limit dominates the phase behavior. This result is not at all obvious as, for rods with this length, the Onsager assumption that all higher virial coefficients are negligible is not yet satisfied.[36] Yet, we cannot rule out the possibility that the discrepancy at higher L/D (lower D/L) is an effect of higher virial coefficients. The agreement at lower L/D values should then be attributed to a fortuitous cancellation of errors.

Of course, the nematic-to-smectic and smectic-to-solid transition are more difficult to study, because they occur at higher density. This has two consequences: first of all, higher density means more particles in a box of a given (minimum) size, and second, equilibration at high densities is slower. For $L/D = 40$ the equation of state is plotted in Fig. 13. We estimate that the reduced densities of the coexisting smectic and solid phases are $\rho^*=0.66$ and $\rho^*=0.68$, respectively. The nematic-smectic transition is estimated to take place at about $\rho^*=0.5$. However, it is difficult to locate this transition accurately, as the smectic fluctuations in the nematic phase decay extremely slowly, even at lower densities. Poniewierski[37] has studied the nematic-to-smectic transition in the Onsager limit using bifurcation analysis. He found that the bifurcation point of the nematic-smectic transition is lo-

TABLE XII. Pressure, densities, and nematic order parameters of coexisting isotropic and nematic phases for hard spherocylinders with shape anisotropies L/D between 20 and 60. The coexistence data in this table were obtained using Gibbs-ensemble simulations. Units as in Table III.

L/D	Pv_0/kT	ρ_{iso}^*	ρ_{nem}^*	S_I	S_N
20	0.037 63	0.1518	0.1915	0.093	0.872
30	0.024 95	0.1036	0.1201	0.055	0.743
40	0.012 63	0.0818	0.1044	0.098	0.844
50	0.005 82	0.0638	0.0763	0.192	0.736
60	0.003 28	0.0535	0.0615	0.057	0.703

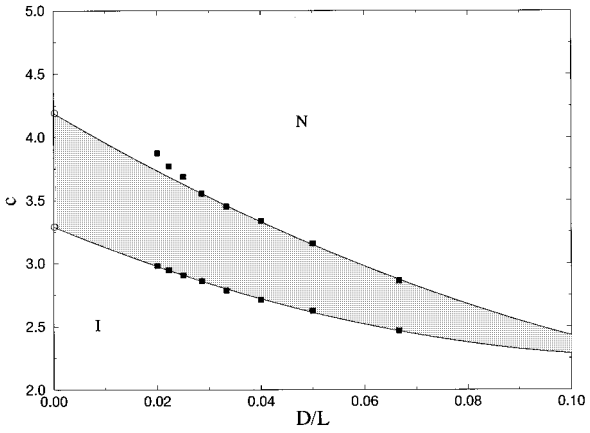

FIG. 12. Isotropic-nematic transition of spherocylinders in the large L/D limit. In order to facilitate comparison with the Onsager limit, all densities are expressed in units $c=\frac{1}{4}\pi L^2 D\rho$. On the x axis, we plot D/L rather than L/D. Hence, the Onsager limit corresponds to the value $D/L=0$. Note that our simulation results approach smoothly towards the exact solution of the Onsager model, except for a few points at low D/L.

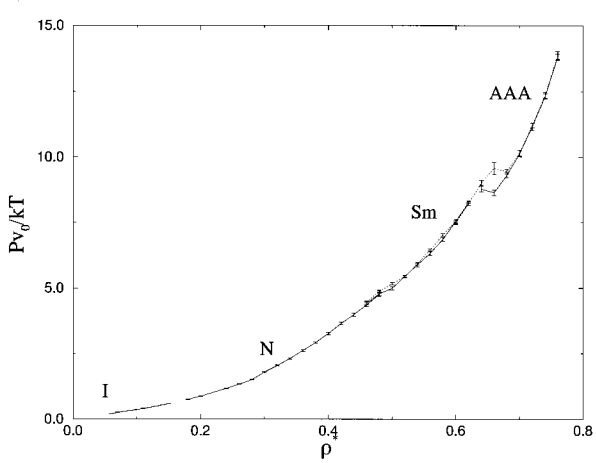

FIG. 13. Equation of state for spherocylinders with shape anisotropy $L/D=40$. The dashed curves correspond to a compression whereas the solid curves denote an expansion. The different mechanically stable phases are indicated. All units as in Fig. 4.

cated at $\rho LD^2=0.531$ which corresponds to a reduced density $\rho^*=0.46$. This agrees with the decreasing trend in the transition density if one goes from $L/D=5$ to $L/D=40$. However, it also shows that the N-SmA transition for $L/D=40$ is significantly different from the transition at $L/D\rightarrow\infty$.

In Fig. 2 we have combined our results for the phase behavior at large L/D values with the low L/D phase diagram discussed before. In order to give equal emphasis to all parts of the phase diagram, we have plotted the figure in the $(\rho^*,\log(L/D+1))$ plane.

C. The AAA crystal phase

For lengths larger than approximately seven a hexagonal crystal phase develops between the smectic and ABC-stacked solid phase. This crystal phase is characterized by hexagonally ordered layers which are stacked in an ''AAA'' fashion. That is, a particle's hemisphere is right above the end cap of a particle in the layer below it. In contrast, an fcc crystal is stacked in an ''ABC'' manner, with the particles end caps in one layer shifted with respect to the next layer (see Fig. 14). The ''AAA'' crystal is more stable than the ABC crystal because the particles have a larger free volume. If they move along the z direction they will on average only hit the particle right above or below. In the ABC stacking the number of interactions is much larger because the layers are shifted in position with respect to each other. At higher densities, the end caps of particles in neighboring layers start to feel each other and the AAA-stacked crystal will transform again to the ABC stacking. A rough but simple estimate for the AAA-ABC transition density can be made as follows. The reduced density of a crystal can be written in terms of the expansion from a close-packed crystal:

$$\rho^*=\frac{1}{(1+a_z)(1+a_{xy})^2}, \tag{50}$$

where a_z+1 is the expansion of the lattice in the z direction starting, whereas $a_{xy}+1$ is the expansion in the xy plane. Because the particles are uniaxial, the expansion in the x and y plane are equal (compare Sec. V B). The z direction expansion has, in general, a different value. From simulation results we can deduce that $a_{xy}\approx 2a_z$. Further, the expansion $1+a_z$ can be expressed as the ratio of the real box length and the close-packed crystal box length in the z direction:

$$1+a_z=\frac{\Delta/D+L/D}{L/D+\sqrt{\frac{2}{3}}}=\frac{\Delta/D-\sqrt{\frac{2}{3}}}{L/D+\sqrt{\frac{2}{3}}}+1. \tag{51}$$

Here Δ is the interlayer spacing. We assume that the AAA-ABC transition takes place when the distance between layers Δ is of the order of the diameter D. At that moment the end caps definitely start to feel each other and an ABC stacking is more favorable. This results in an estimate for the reduced transition density

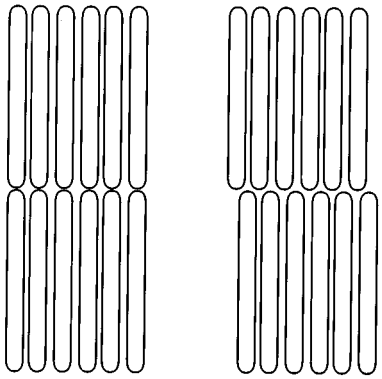

FIG. 14. Cartoon of the major difference between the AAA and the ABC stacking. Left: In the AAA stacking every particle is right on top of a particle in the layer below. Right: In the ABC stacking the layers are shifted.

$$\rho^{*-1} \approx \left(1 + 2\frac{1-\sqrt{\frac{2}{3}}}{L/D+\sqrt{\frac{2}{3}}} \right)^2 \left(1 + \frac{1-\sqrt{\frac{2}{3}}}{L/D+\sqrt{\frac{2}{3}}} \right). \quad (52)$$

This density is plotted in Fig. 2. We could also estimate the AAA-ABC transition for $L/D=10$ and $L/D=20$ from the equations of state in the crystal state. These values are indicated as well in Fig. 2. The agreement is reasonably good and suggests that the argument of the hemispheres and the layer spacing is qualitatively correct.

VII. THE ONSAGER LIMIT

A. Scaling

As we saw in the previous section, spherocylinders with $L/D=40$ are too small to compare properly with the bifurcation results of Poniewierski for $L/D\to\infty$, and so it would be interesting to simulate a system of spherocylinders in this limit. At first sight this seems impossible because in general the system size scales with L^3. However, at finite reduced density ρ^*, i.e., not in the isotropic phase or low ρ^* nematic phase, the average angle θ that a particle makes with the director scales as $1/L$, which means that the particles are (almost) completely aligned. In this regime, we can bring the volume down to finite sizes by scaling the system along the director (chosen to be along the z axis) with a factor L. This will change the shape of the particle from a spherocylinder to a shifted cylinder of height 1 and diameter D (see Fig. 15). The height of the cylinder is always 1 because the angle $\theta \propto 1/L$ and the difference in height $1-\cos(1/L)\approx 1/L^2$ vanishes as $L/D\to\infty$. The shift of the cylinder in the xy plane perpendicular to the director is finite because it is given by $L\sin\theta = \mathcal{O}(\mathcal{D})$ in the limit $L/D\to\infty$. The top and bottom end of the cylinder are flat and always perpendicular to the director. The hemispheres of the spherocylinder have completely disappeared via the scaling procedure.

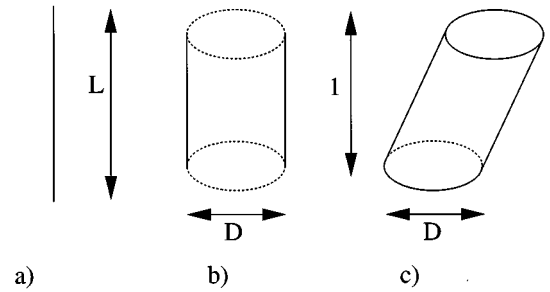

FIG. 15. Scaling of the spherocylinder if $L/D\to\infty$. (a) shows a spherocylinder with finite L and zero D, the tilt angle goes as D/L. (b) is a blown up part of length 1 of spherocylinder a on the scale of diameter D. The cylinder part still looks completely parallel to the z axis because the tilt angle is vanishing. (c) Scaled particle. The particle is scaled by a factor L along the z axis. The hemispheres have vanished, so the upper and lower plane of the cylinder is flat and perpendicular to the z axis. The particle is a shifted cylinder because the total displacement of the unscaled spherocylinder $L\sin\theta \sim L\sin(1/L)\approx 1$, although zero on the L scale, is not zero on the D scale.

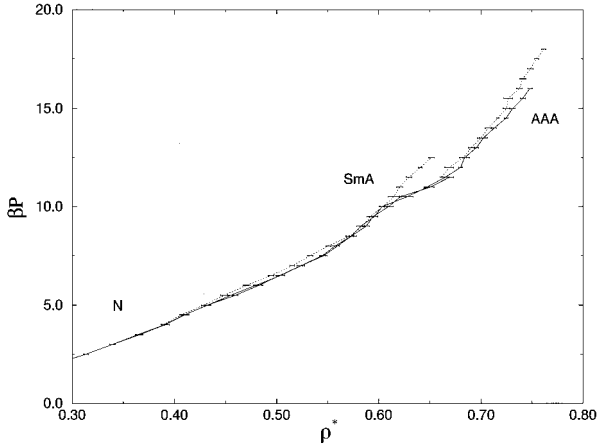

FIG. 16. Equations of state of the spherocylinder system in the limit $L/D\to\infty$. The solid lines are expansion branches, the dotted lines are compression curves. The hysteresis around $\rho^*=0.5$ is suggestive of a first order nematic-to-smectic phase transition.

Because the shape of the particle is different from a spherocylinder we need a new overlap criterion. This is given by the shortest distance between two particle axes in the *xy* plane. In the *xy* plane a cut through the cylinder results in a circle of diameter D. Therefore, if the shortest distance is smaller than the diameter D, an overlap will occur.

Scaling of the box in this particular way will not effect the reduced density because the close-packing density will scale in the same way as the number density. The pressure will be multiplied by a factor L, whereas P/ρ remains uneffected by the scaling. We can therefore measure the equation of state of the Onsager limit system in the normal NPT ensemble.

Because the particles are free to shift any arbitrary amount in the *xy* plane, it is convenient to keep the nematic director always along the *z* axis. That is, we keep the total amount of shift in the *xy* plane equal to zero. This can be achieved by starting with a completely aligned system and shift two particles with the same amount in opposite direction at every MC trial move. In order to avoid multiple overlaps, shifts larger than half the box length are forbidden. Standard MC trial moves were not very effective in reproducing the collective motion of tilted layers. In the smectic phase, we therefore allowed for two neighboring layers to tilt collectively by equal but opposite amounts, so that the constraint of a constant director is satisfied.

B. Results

We prepared a system of 600 cylinders at $\rho^*=0.8$ in an ABC stacking and performed Onsager NPT simulations, first expanding to lower densities and subsequently compressing. The equation of state of spherocylinders in the limit $L/D\to\infty$ is shown in Fig. 16. There is no isotropic phase at finite reduced densities because the I-N transition has shifted down to $\rho^*=0$. Therefore, at all reduced densities below $\rho^*\approx 0.47$ the nematic phase is stable. The nematic-to-smectic transition is estimated to take place at $\rho^*\approx 0.47$.

This is in agreement with the predictions of Poniewierski who located the N-S transition at $\rho^*=0.46$ using bifurcation analysis.[37]

At higher density the smectic phase will be thermodynamically stable, until at $\rho^*\approx 0.66$ the system crystallizes in an AAA stacking. This transition is first order as is clear from the strong hysteresis at $\rho^*\approx 0.66$ in Fig. 16. The system prefers an AAA stacking because the particles are hindered by fewer particles in the neighboring layers than in an AB or ABC stacking and hence have more entropy. The AAA phase will undergo a transition to an ABC crystal only at close packing, because the ABC-stacked lattice will be stabilized only if the distance between layers is of the order of D. At that point the particles start to feel the hemispheres of the particles in the neighboring layers. Because $D/L=0$ this can only happen at close-packing densities.

We also found evidence for a columnar structure between the smectic and the AAA phase. This columnar phase appeared meta-stable with respect to the AAA crystal.

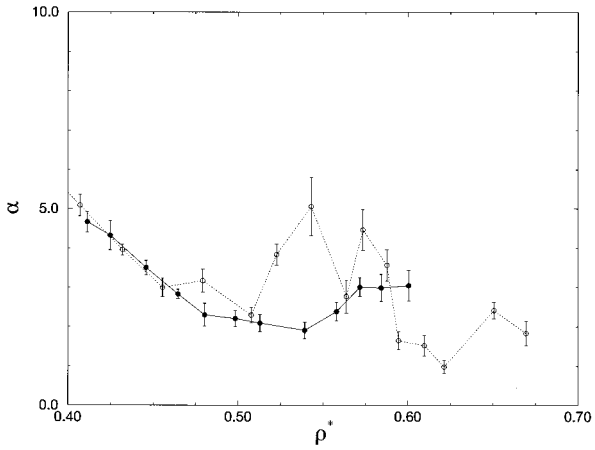

FIG. 17. The measure for nematic order α in an Onsager spherocylinder system as a function of reduced density ρ for a compression from the nematic (filled circles) and an expansion from the smectic phase (open circles). Note the clear hysteresis.

C. What is the order of the nematic-smectic transition?

It is usually assumed that the nematic-to-smectic transition in the Onsager limit is continuous. However, there is no hard (theoretical) evidence to support this conjecture. On the contrary, although Poniewierski performed his theoretical analysis assuming a continuous N-S transition, he pointed out that a (weak) coupling between orientation and translational degrees of freedom would make the transition first order.[37] We tried to determine the order of the nematic-to-smectic transition numerically. The results appear to depend on the type of periodic boundaries used in the simulations. In the case of normal periodic boundaries, we found evidence for a first order N-S transition, whereas by applying shifted periodic boundary conditions as described in Sec. III B 3, the transition becomes continuous.

1. Normal periodic boundaries

The hysteresis at densities around $\rho^*=0.5$ between the compression and expansion branch in Fig. 16 is an indication for a first order N-S transition. When we consider the nematic order parameter of the system, this hysteresis becomes even more clear. In the limit $L/D\rightarrow\infty$ the nematic order parameter can be written to leading order in D/L as

$$S=1-\frac{3}{2}\langle\sin^2\theta\rangle=1-\frac{3}{2}\langle u_x^2+u_y^2\rangle\frac{D^2}{L^2}\equiv 1-\frac{3}{2}\,\alpha\,\frac{D^2}{L^2}, \tag{53}$$

where θ is the angle the particles make with the director and the latter equation defines α as the mean-square shift of the cylinders. In Fig. 17 we plotted the measured value of α as a function of the reduced density for both the compression and expansion branches. The most remarkable feature is that near the transition α is larger in the smectic phase than in the nematic. This corresponds to a more orientational ordered nematic at lower densities and a less ordered smectic at higher density. There is a competition between translational and orientational entropy. In the nematic phase the translational entropy is large but the rods are restricted in their rotations. On the other hand, in the smectic phase, the layering increases the orientational entropy increases, which manifests itself as herringbone fluctuations of the smectic layers. Figure 17 also clearly shows the hysteresis between the compression and expansion branches. The compression from the nematic phase shows only increasing disorder for $\rho^*>0.54$ whereas α in the case of the expansion from the smectic drops to low value below $\rho=0.5$. The two examples of hysteresis given above suggests that we have a first order transition. However, as before, only free-energy calculations can locate the exact transition. We performed free-energy difference calculations as described in Sec. III B 4 to estimate the free-energy difference between an nematic Onsager system at $\rho^*=0.4$ and a smectic at $\rho^*=0.5$. Those calculations did not result in reasonable values for the nematic-smectic coexistence densities.

2. Shifted periodic boundaries

The transition could be second order and the hysteresis might be due to a slow relaxation to the equilibrium state. The rate of relaxation is determined by the exchange of molecules between the smectic layers during compression from the nematic phase. This diffusion becomes inefficient at higher pressure. To circumvent this problem we have applied the shifted periodic boundary conditions to the Onsager system (see Sec. III B 3) and determined the compression and expansion curves again. The results are plotted in Fig. 18. These equations of state seem to indicate that the nematic-smectic transition is continuous in the Onsager limit. The continuity also follows from Fig. 19 where α, our measure for nematic order, is plotted against the reduced density. However, the shifted periodic boundaries suppress the herringbone structured smectic fluctuations phase and inclusion of these fluctuations could make the transition (weakly) first order again.

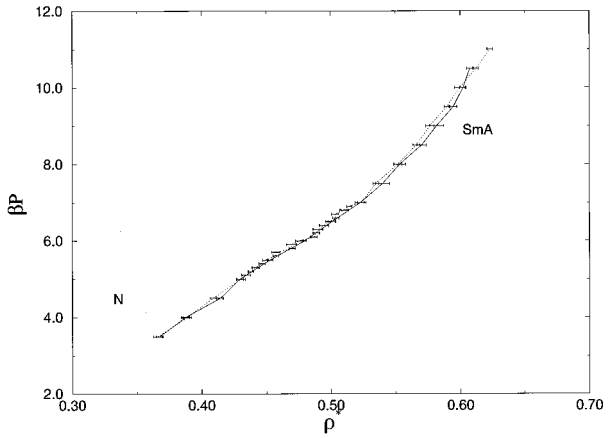

FIG. 18. Equations of state around the nematic-to-smectic transition of the spherocylinder system in the limit $L/D\rightarrow\infty$. The solid line is the equation of state for the expansion from a smectic, the dotted line is the compression curve started from the nematic. The hysteresis has disappeared due to the use of shifted periodic boundaries.

In short, we cannot establish with certainty the order of the N-S transition in the limit $L/D\rightarrow\infty$. To establish the nature of the transition, a full finite size scaling analysis is required. As the shifted periodic boundary conditions simulation offer better statistics, we tend to believe that the N-S transition is continuous. Since the transition *is* clearly first order for $L/D=5$, there should be a tricritical point at intermediate L/D. This tricritical point has been the subject of theoretical studies. In Refs. 17 and 18 it is estimated that the tricritical point corresponds to $L/D\approx 5$ while the theoretical analysis in Ref. 19 suggest that it should occur at $L/D=50$. The first prediction is clearly incompatible with our simulation results and those of Ref. 15.

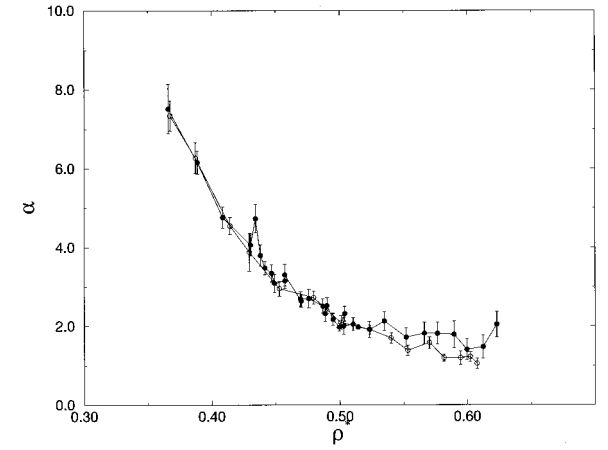

FIG. 19. The measure for nematic order α in an onsager spherocylinder system as a function of reduced density ρ for a compression from the nematic (filled circles) and an expansion from the smectic phase (open circles). The hysteresis has disappeared due to the use of shifted periodic boundaries.

VIII. CONCLUSIONS

In summary, we have mapped out the spherocylinder phase diagram over a wide range of densities and L/D values, such that it was possible to establish the link with the hard-sphere phase diagram for small L/D and with the Onsager limit for $L/D\rightarrow\infty$. We find that the liquid crystalline nematic phase is stable from about $L/D\approx 3.7$. The isotropic nematic coexistence decreases as a function of L/D and follows the Onsager theory in the $L\rightarrow\infty$ limit.

The smectic phase becomes stable at $L/D\approx 3.1$. The isotropic-smectic and later on the nematic-smectic transition starts off as a strong first order transition for $L/D>3.7$. The density jump becomes smaller at higher L/D. For $L/D\approx 7$ the AAA-stacked crystalline phase becomes stable. The AAA-ABC transition was found to be first order. The transition density increases with L/D and reaches close packing in the Onsager limit. Between $L/D=4$ and $L/D=\infty$ the first order smectic–solid transition is located at the almost constant reduced densities $\rho^*_{\mathrm{smect}}=0.66$ and $\rho^*_{\mathrm{solid}}=0.68$. We determined the phase behavior of spherocylinders in the Onsager limit and estimated the location of the nematic-to-smectic phase at $\rho^*=0.47$, which is in agreement with the predicted value of $\rho^*=0.46$. In order to establish the link between the Onsager limit and the phase behavior for finite spherocylinders, we plotted in Fig. 20 the phase diagram as a function of D/L.

We stress that the phase diagram of long rods does not only depend on L/D, but also on the exact shape of the particle. For instance, hard ellipsoidal particles do not form a stable smectic phase, even in the Onsager limit, whereas hard spherocylinders clearly do. When comparing with experiments[14] this should be kept in mind. The rotator-to-solid phase transition at low L/D was calculated and appeared to be strongly dominated by the behavior in the close-packed limit. In the calculations we used three nonstandard simulation techniques:

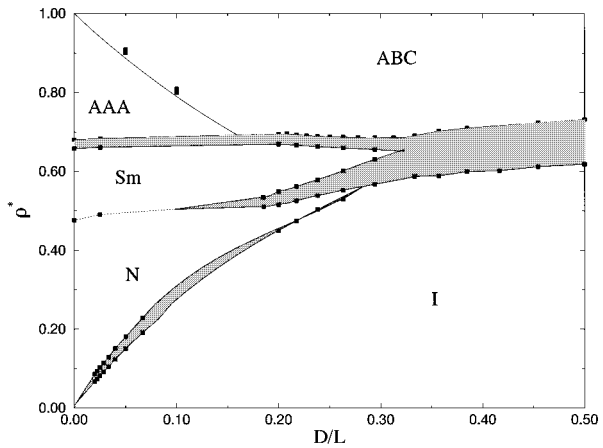

FIG. 20. The phase diagram of hard spherocylinders plotted as a function of D/L. In this way we can establish the link between the finite length region and the Onsager limit at $D/L=0$.

- The Gibbs–Duhem integration method of Kofke was modified to compute the L/D dependence of phase-coexistence curves.
- The plastic-rotator transition was investigated in the close-packing limit by mapping the system onto a special lattice model.
- The Onsager limit was studied by scaling the infinitely long particles to finite length.

ACKNOWLEDGMENTS

We thank Richard Sear and René van Roij for a critical reading of the manuscript and George Jackson for sending us a preprint of Ref. 15. The work of the FOM Institute is part of the research program of FOM and is made possible by financial support from the Netherlands Organization for Scientific Research (NWO).

[1] L. Onsager, Ann. N.Y. Acad. Sci. **51**, 445 (1949).
[2] B. J. Alder and T. A. Wainwright, J. Chem. Phys. **27**, 1208 (1957).
[3] W. W. Wood and J. D. Jacobson, J. Chem. Phys. **27**, 1207 (1957).
[4] J. Vieillard-Baron, Mol. Phys. **28**, 809 (1974).
[5] D. Frenkel and B. M. Mulder, Mol. Phys. **55**, 1171 (1985).
[6] A. Stroobants, H. N. W. Lekkerkerker, and D. Frenkel, Phys. Rev. A **36**, 2929 (1987).
[7] D. Frenkel, J. Phys. Chem. **91**, 4912 (1987).
[8] D. Frenkel, H. N. W. Lekkerkerker, and A. Stroobants, Nature **332**, 882 (1988).
[9] J. A. C. Veerman and D. Frenkel, Phys. Rev. A **41**, 3237 (1990).
[10] D. Frenkel, Liq. Cryst. **5**, 929 (1989).
[11] J. A. C. Veerman and D. Frenkel, Phys. Rev. A **45**, 5633 (1992).
[12] M. P. Allen, G. T. Evans, D. Frenkel, and B. M. Mulder, Adv. Chem. Phys. **86**, 1 (1993).
[13] H. N. W. Lekkerkerker, P. Buining, J. Buitenhuis, G. J. Vroege, and A. Stroobants, in *Observation, Prediction and Simulation of Phase Transitions in Complex Fluids*, NATO ASI series C, Vol. 460, edited by M. Baus, L. F. Rull, and J. P. Ryckaert (Kluwer Academic, Dordrecht, 1995).
[14] S. Fraden, in *Observation, Prediction and Simulation of Phase Transitions in Complex Fluids*, NATO ASI series C, Vol. 460, edited by M. Baus, L. F. Rull, and J. P. Ryckaert (Kluwer Academic, Dordrecht, 1995).
[15] S. C. McGrother, D. C. Williamson, and G. Jackson, J. Chem. Phys. **104**, 6755 (1996).
[16] P. G. Bolhuis, M. H. J. Hagen, and D. Frenkel, Phys. Rev. E **50**, 4880 (1994).
[17] A. Poniewierski and R. Holyst, Phys. Rev. A **41**, 6871 (1990).
[18] A. Poniewierski and T. J. Sluckin, Phys. Rev. A **43**, 6837 (1991).
[19] A. M. Somoza and P. Tarazona, Phys. Rev. A **41**, 965 (1990).
[20] D. A. Kofke, J. Chem. Phys. **98**, 4149 (1993).
[21] S. D. Hudson and R. G. Larson, Phys. Rev. Lett. **70**, 2916 (1993).
[22] R. van Roij, P. G. Bolhuis, B. Mulder, and D. Frenkel, Phys. Rev. E **52**, R1277 (1995).
[23] D. W. Rebertus and K. M. Sando, J. Chem. Phys. **67**, 2587 (1977).
[24] M. P. Allen, D. Frenkel, and J. Talbot, Comp. Phys. Rep. **9**, 301 (1989).
[25] D. Frenkel and A. J. C. Ladd, J. Chem. Phys. **87**, 3188 (1984).
[26] W. G. Hoover and F. H. Ree, J. Chem. Phys. **49**, 3609 (1968).
[27] S. J. Singer and R. Mumaugh, J. Chem. Phys. **93**, 1278 (1990).
[28] C. Vega, E. P. A. Paras, and P. A. Monson, J. Chem. Phys. **96**, 9060 (1992).
[29] C. Vega, E. P. A. Paras, and P. A. Monson, J. Chem. Phys. **97**, 8543 (1992).
[30] J. A. Zollweg and G. V. Chester, Phys. Rev. B **46**, 11 187 (1992).
[31] L. D. Landau and E. M. Lifshitz, *Statistical Physics*, 3rd ed., revised by E. M Lifshitz and L. P. Pitaevskii (Pergamon, Oxford, 1980).
[32] R. Hall, J. Chem. Phys. **57**, 2252 (1972).
[33] A. Z. Panagiotopolous, Mol. Phys. **61**, 813 (1987); A. Z. Panagiotopolous, N. Quirke, M. Stapleton, and D.J. Tildesley, Mol. Phys. **3**, 527 (1988).
[34] B. Smit, Ph. de Smedt, and D. Frenkel, Mol. Phys. **68**, 931 (1989).
[35] H. N. W. Lekkerkerker, P. Coulon, R. van der Haegen, and R. Deblieck, J. Chem. Phys. **80**, 3427 (1984).
[36] D. Frenkel, J. Phys. Chem. **91**, 4912 (1987); **92**, 5314 (E) (1988).
[37] A. Ponierwierski, Phys. Rev. A **45**, 5605 (1992).